Synergistic Diffuser/Heat-Exchanger Design

by

David S. Lazzara

B.S., University of Southern California (2002)

Submitted to the Department of Aeronautics and Astronautics
in partial fulfillment of the requirements for the degree of

Master of Science in Aeronautical and Astronautical Engineering

at the

MASSACHUSETTS INSTITUTE OF TECHNOLOGY

May 2004

Author .....
Department of Aeronautics and Astronautics
May 7, 2004

Certified by .....
Mark Drela
Terry J. Kohler Professor of Fluid Dynamics
Thesis Supervisor

Accepted by .....
Edward M. Greitzer
H.N. Slater Professor of Aeronautics and Astronautics Chair,
Committee on Graduate Students

Synergistic Diffuser/Heat-Exchanger Design

by

David S. Lazzara

Submitted to the Department of Aeronautics and Astronautics
on May 7, 2004, in partial fulfillment of the
requirements for the degree of
Master of Science in Aeronautical and Astronautical Engineering

Abstract

The theoretical and numerical evaluation of synergistic diffusing heat-exchanger design is presented. Motivation for this development is based on current diffuser and heat-exchange technologies in cogeneration plants, which require a large geometric footprint to generate steam using gas-turbine exhaust. A compact design is hypothesized to replace these technologies using synergistic design concepts. An investigation into the feasibility of such design concepts are conducted, providing pressure-recovery, viscous losses and thermal energy extraction sensitivities to cooling and annular blade geometry variations. Results show promising diffusion and heat-transfer capabilities that match or surpass current design performance. Proposed configurations are outlined based on these results that compare favorably to a baseline industrial cogeneration application.

Thesis Supervisor: Mark Drela
Title: Terry J. Kohler Professor of Fluid Dynamics

Acknowledgments

I express much gratitude to my thesis advisor, Mark Drela, for his assistance and support throughout the progression of this research project. Many thanks are also given to the Aerospace Computational Design Lab at MIT for the facilities they provided to conduct this work and the amiable environment its members sustained.

It is with sincere appreciation that I thank God, my family and extended relatives for the continual support, encouragement and positive reinforcement they provided each day, regardless of my shortcomings and small successes. Their love is always cherished.

Contents

List of Figures

List of Tables

Chapter 1

Introduction

The concept of synergistic diffuser and heat-exchanger design is presented in this paper. Its motivation derives from direct application to the diffusion and heat-recovery processes in cogeneration plants. Current cogeneration cycles diffuse high velocity gas-turbine exhaust for thermal energy extraction to produce steam. However, the additional diffusion tunnel and large convective heat-exchangers magnify the geometrical footprint of the gas-turbine system substantially, which results in higher up-front costs. A synergistic diffusing heat-exchanger can minimize this footprint and provide equal or better performance.

Diffuser and heat-exchanger design methodologies are provided as a foundation to synergistic design. The idea that heat-exchange complements diffusion is not new, though [4, p. 460]. Its direct application as a boundary-layer control method is historically lacking in comparison to suction or blowing methods [5, p. 382]. Yet, theoretically, boundary-layer stabilization is possible when the wall temperature is less than the flow total temperature. This theory is presented in conjunction with typical diffuser and heat-recovery designs in chapter 2.

After outlining how heat-transfer can improve the diffusion process, chapter 3 presents a set of numerical experiments whereby the synergistic design concept is evaluated. Comparisons between adiabatic and non-adiabatic diffusion demonstrate concept feasibility. An exploration of the geometrical design space is also provided to understand how blade geometry couples with cooling to assist or deter diffusion and

heat-recovery. These parameters are judged on the basis of pressure-recovery, viscous loss minimization and total-enthalpy reduction in the flow.

Finally, chapter 4 applies synergistic design to replace an existing heat-recovery system. A short summary of the existing system is given to define minimum performance thresholds in diffusion and thermal energy extraction. Trade-offs encountered in applied synergistic design are set forth as well. These provide the reasoning behind two proposed diffusing heat-exchanger configurations. A look at how plant steam processing requirements determine the heat-recovery design is also given. Additional system-level design considerations are posed in summary form to direct future work in the area of synergistic diffusion heat-recovery design.

Chapter 2

The Cogeneration Problem

An outline of current cogeneration heat-recovery systems and their design methodology are introduced in the following sections to provide a motivation for a synergistic design concept. A brief look at both diffuser and heat-exchanger design, at the system level, are also given as a precursor to design considerations that combine their functions. These synergistic design considerations are then explained by means of boundary-layer theory. The fundamental flow physics explained by this theory provides objectives for numerically validating the synergistic design concept.

2.1 Cogeneration Systems

Many modern-day electric power plants utilize a combined gas-turbine and steam-turbine installation to drive an electric generator and provide steam for plant processes. Depending on the steam and power generation constraints, the gas-turbine is sized for minimal fuel input and maximum shaft work. Unlike aircraft power generation, ground-based gas-turbines and heat-exchangers are not restricted to minimum weight or geometrical constraints. For this reason, the plant designer is at liberty to match the customer's increasing steam and power needs to a gas-turbine system with a substantial volumetric footprint.

Greater engine mass-flow can increase power generation. Steam production, however, entails the use of large convective heat-exchangers that extract thermal energy

from the high temperature gas-turbine exhaust. The exhaust thermal energy cannot be utilized by any other means. Furthermore, a requirement for superheated steam results in even larger surface-area heat-exchangers, or the addition of heat-exchangers in series. These system add-ons can increase the gas-turbine system installation by 100%, or more, and result in substantial system complexity. An example configuration is presented in figure 2-1, which denotes the relative geometrical footprint of the heat-recovery and gas-turbine systems in a Solar Turbine Titan 130 [7].

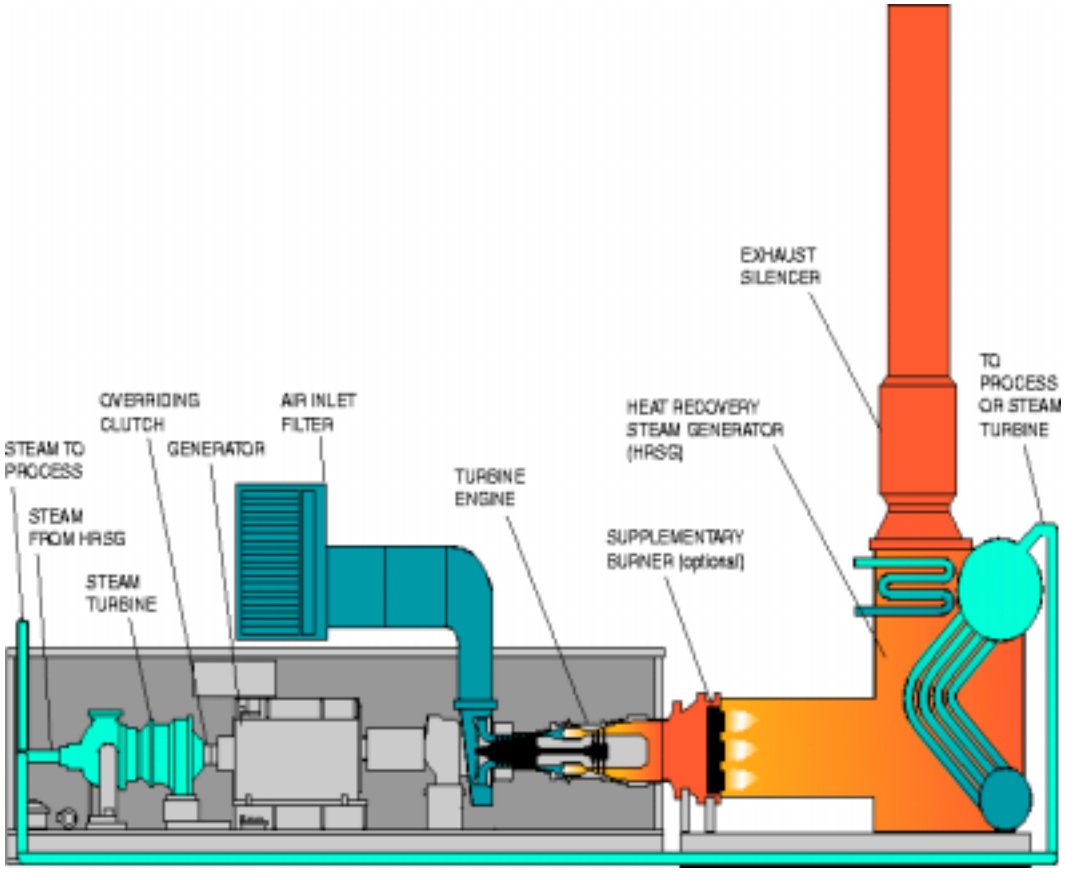

Figure 2-1: The Solar Turbine Titan 130 Steam-Turbine Assisted Cogeneration system.

2.2 Current Cogeneration Design

The current power and steam generation design methodology separates the cogeneration problem into two smaller design studies: 1) the power generation problem, and 2)

the heat-transfer problem. The separate design considerations contain a common interface, namely that of a diffuser that links the turbine exhaust to the heat-exchanger inlet. This essential component translates the exhaust kinetic energy into a static-pressure rise. Decreasing the exhaust velocity in this manner improves heat-transfer within the heat-exchanger.

At first glance it appears that the cogeneration problem is easily solved by designing the gas-turbine to match power generation needs, sizing a heat-exchanger for proper steam generation and finally creating a diffuser that can unite the distinct flow conditions between the two components.

This proven design methodology allows for enhancements in separate gas-turbine and heat-exchanger technologies. However, adding a geometrical constraint to the design problem requires a different approach. Power generation necessitates a minimum engine mass-flow that essentially minimizes the gas-turbine geometry. Since the addition of steam-generation components increases the installation footprint of the gas-turbine system by at least 100%, initial technology improvements should minimize the diffuser and heat-exchanger geometry while providing equal (or better) steam generation performance.

2.3 Proposed Cogeneration Design Method

An improved cogeneration design method requires a unique solution to the heat-transfer problem while minimizing heat-exchanger geometry. A proposed solution uses synergistic diffuser and heat-exchanger design. This concept combines the diffuser and heat-exchanger components into a single entity that accomplishes both static-pressure rise and heat extraction. An annular set of turning vanes provide diffusion and also extract heat via internal passing of cooling water (in a compressed liquid, saturated, or superheated vapor thermodynamic state). The new component could dramatically reduce the geometrical footprint of a power and steam generation installation, and thereby decrease unit costs and reduce system complexity.

Dividing the cogeneration problem into two smaller problems is still possible;

but this only allows the design of a new diffusing heat-exchanger that matches the performance of current steam generating components. If greater diffusion is achieved, the gas-turbine can likewise accelerate the working fluid to lower static-pressures and generate more power. The same exhaust pressure can be obtained aft of the heat-exchanger, as in current designs, based on the improved diffusion capability. It is apparent that such a design requires an iterative approach due to the performance coupling between the gas-turbine and diffusing heat-exchanger.

In order to see the performance benefits of a diffusing heat-exchanger, the facets of a typical diffuser and heat-exchanger design need delineation first.

2.3.1 Diffuser Design Considerations

Diffuser designs were historically derived using empirical methods [8, p. 381]. A poor theoretical understanding of flow stall on diffuser walls forced diffuser designers to rely on rules-of-thumb rather than scientific fundamentals. Five diffuser parameters were often varied in order to find an optimum pressure recovery based on the inlet flow conditions:

1. Aspect Ratio
2. Cross-sectional geometry
3. Inlet-Exit area ratio
4. Expansion angle
5. Inlet boundary-layer blockage

Regardless of the diffuser configuration, the most important performance parameter is the pressure recovery, C_p, defined as

$$C_p = \frac{p_2 - p_1}{p_{t_1} - p_1}. \tag{2.1}$$

C_p provides a ratio of the static-pressure achieved aft of the diffuser to that theoretical pressure obtained by adiabatic and isentropic flow deceleration to zero kinetic

energy (i.e., stagnation pressure). This parameter is heavily dependent on the diffuser configuration. High C_p values (typically 0.8) are usually obtained using long diffuser tunnels with low expansion wall angles. Low C_p values (about 0.4) are often a result of short diffusers with low inlet-exit area ratios and high expansion angles. As diffuser geometry is shortened, the exit flow conditions approach that of a jet–where complete stall of all diffuser walls exists. The same occurs if the expansion angle is too large. Before the jet condition is reached, though, the flow stalls asymmetrically in the diffuser. In this case the flow stalls on only a portion of the diffuser wetted area, or the flow may oscillate between stall behavior on opposing walls as well (transitory stall). Experimental evidence suggests that the highest C_p is obtained in the transitory stall flow regime [8, p. 383].

Foreseeing the potential C_p impact caused by a change in diffuser geometry is difficult because viscous diffuser flows do not provide the pressure recovery predicted by inviscid flow analysis. Boundary-layer theory provides insight into the coupling between the diffuser core potential flow and its wall boundary-layers. Thus, modern computational fluid dynamics codes improve the understanding of diffuser flow prior to testing. These codes document performance sensitivities to geometry changes and predict stall.

Diffuser cross-sectional geometry and inlet-exit areas are often dictated by the given inlet and desired exit conditions. Rectangular and circular cross-sections are the most common. In other cases an annular diffuser is preferred. This geometry is selected in gas-turbine applications for exhaust diffusion. An important design consideration for annular diffusers pertains to inlet flow swirl angles. Flow breakdown can easily occur within an annular diffuser due to strong swirl susceptibility, which creates a free vortex around a low-pressure core. High-pressure flow downstream may reverse into this core and cause flow breakdown [10, pp. 173-175].

2.3.2 Heat-Exchanger Design Considerations

Forced convective heat-transfer is the primary means of heat-exchange for steam production. A Waste Heat Recovery Boiler is the collection of heat-exchangers that

change the water coolant enthalpy from a condensed liquid to that of a saturated or superheated vapor. Although radiation is another form of heat-transfer that occurs between the hot turbine exhaust and coolant fluid, its associated heat-transfer coefficient can be at least an order of magnitude smaller than that of forced convection. Once the steam exit conditions are defined (based on coolant inlet conditions) and the turbine exhaust flow is known, a thermodynamic balance of each waste heat recovery component is used to calculate the heat-transfer rate.

Waste heat recovery boilers contain the following major heat-exchange subsystems, which are typically optimized individually:

1. Economizer
2. Evaporator
3. Superheater

Temperature variations between the coolant and exhaust gas are shown in figure 2-2 for each subsystem, which is adapted from Li & Priddy [3, p. 544]. The economizer is configured to increase the inlet coolant enthalpy from a compressed liquid to a saturated liquid state. This process, as are all of the heat-exchanger internal processes, is assumed to occur at a constant coolant pressure. A saturated liquid state may not be obtained (if desired) in order to reserve the steaming process for the evaporator. The relatively low coolant enthalpy (with respect to saturation enthalpy) entering the economizer allows placement at the aft end of the waste heat recovery boiler, where turbine exhaust has already been substantially cooled. By maintaining a temperature difference in this manner, the economizer extracts as much remaining thermal energy as possible (limited by surface area) before gases exhaust through a stack.

The evaporator, or boiler, increases the saturated liquid enthalpy to that of a saturated vapor state. Some plants utilize supplementary firing to increase the finite temperature difference between the turbine exhaust and the saturated liquid. The heat-exchanger pinch point is defined in the evaporator as well, where the smallest difference between the exhaust gas and saturated liquid temperatures exists. A

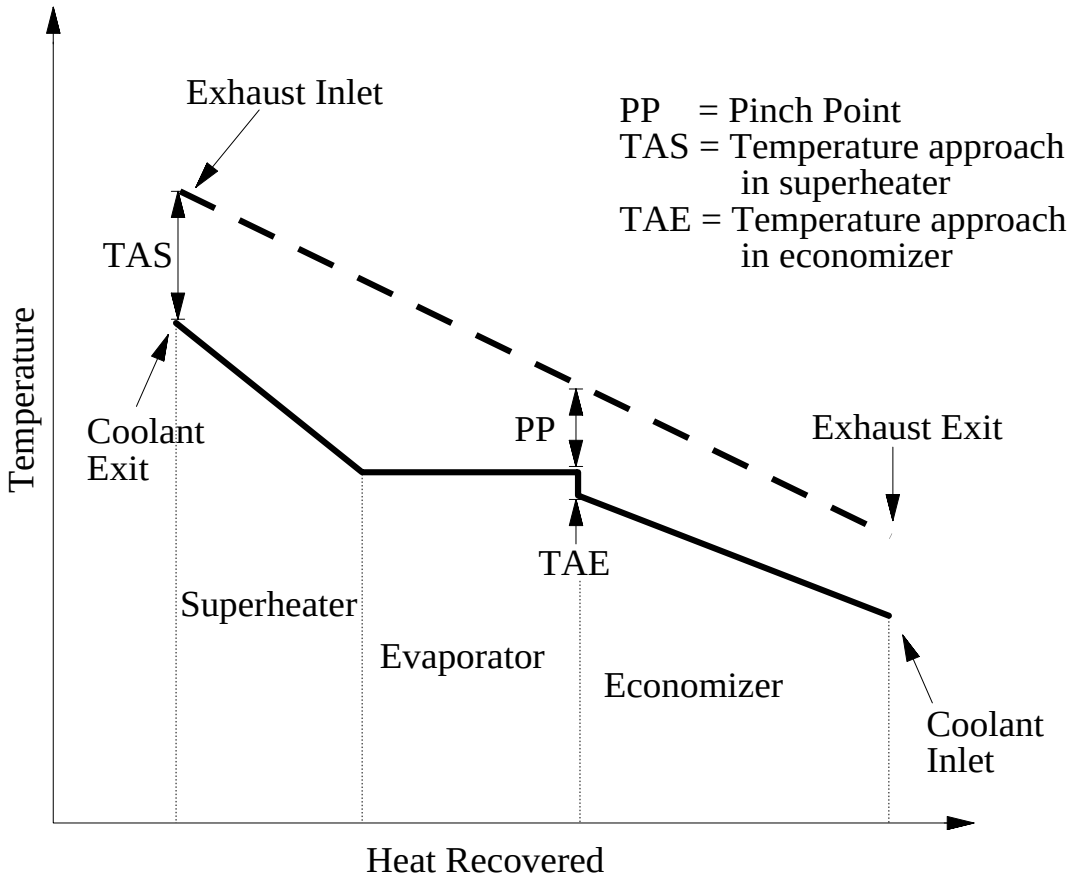

Figure 2-2: Typical temperature profile within a waste heat-recovery system.

lower pinch point requires a larger evaporator (greater heat-transfer surface area); the opposite is true for a higher pinch point.

If the plant requires steam processing conditions beyond that of a saturated vapor, then a superheater is necessary. A superheater increases the steam enthalpy beyond that of a saturated vapor. In order for the superheater steam to have a lower temperature than the surrounding exhaust gas, the superheater is often located near the high temperature turbine exit.

When considering the heat-recovery system as a whole, typical design parameters include [3, p. 544]:

1. Back pressure
2. Pinch point
3. Stack temperature
4. Steam pressure and temperature
5. Superheater and economizer temperature approach

Due to a viscous pressure drop across the waste heat recovery system, the gas-turbine power output suffers an approximate 0.3% power loss for every inch of water increase in back pressure [3, p. 544]. The loss is fixed unless an improved diffuser can compensate by decelerating the turbine exhaust to a higher static-pressure at the heat recovery inlet.

The pinch point indicates the smallest temperature difference between coolant and exhaust gas in the waste heat recovery system. As this value diminishes, more waste heat is recovered. However, a trade-off occurs because the heat-exchange surface area, A, is inversely proportional to the temperature difference, ΔT:

$$A = \frac{q}{U\Delta T}. \tag{2.2}$$

q and U are defined as the heat rate and heat-transfer coefficient, respectively. The stack temperature parameter is involved in a similar trade-off consideration. A stack

exhausts the cooled gas leaving the heat recovery boiler to ambient conditions. Lowering the stack temperature results in better waste heat recovery; yet, based on the argument for pinch point compromise, this requires greater surface area in the economizer because it is the last heat-exchanging component. Any increases in component surface area are balanced by an increase in unit purchasing price [3, p. 545].

The temperature approach in a superheater is defined as the difference in turbine exhaust gas and superheated steam temperatures at the heat-exchanger inlet. An economizer temperature approach is the temperature difference between water saturation temperature and the economizer water exit temperature. The evaporator needs to make up for this temperature difference before steaming can take place. A debate still exists regarding the benefits of a zero economizer approach; arguments are based on avoidance of water hammer and steam blanketing inside the economizer, which can lead to corrosion high maintenance costs [3, p. 546].

Other design considerations include using a dual-pressure boiler, which yields high pressure superheated steam and low pressure saturated steam. This installation has an improved heat rate, yet requires unique design for each distinct plant and is not readily available [3, p. 547]. Another heat recovery option includes supplemental firing in the boiler section. This increases the turbine exhaust temperature and permits the use of larger steam turbines. It also acts as a throttle that maintains steam temperature and pressure when turbine load fluctuates.

There are more detailed design considerations to examine, such as feed-water pump efficiencies and condenser systems. Yet the work required in these systems is a fraction of the heat rate in the boiler and turbine power output. Preliminary design considerations can give order-of-magnitude performance estimates without including these details.

2.4 Synergistic Design Considerations

The preliminary design of a diffusing waste heat recovery boiler can rely on design considerations similar to the individual heat-exchanger and diffuser. Proper trade-

studies are required to identify the sensitivity of C_p to different heat-exchange rates. These studies are magnified when including variations in component geometry and turbine exhaust conditions. Furthermore, sensitivity to the steam production requirements may exist as well. Results must complement a minimization of geometry while maintaining minimum performance expectations.

Economizer, evaporator and superheater roles will need proper attention in the diffusing boiler, in addition to considerations of back pressure influence on the turbine exhaust conditions. An understanding of turbine power output dependence on pressure recovery would yield optimum turbine and boiler matching. However, if the diffusing boiler is an appendage to an existing gas-turbine installation, the pressure recovery does not need to exceed the current design performance. This iterative design process is necessary for each combination of turbine power requirements and steam processing needs unless clear design trends become evident.

Before delving into the configuration-level discussion, the fluid physics that permit a synergistic design must be addressed as the initial step in this development.

2.4.1 Boundary-Layer Theory Applied to a Diffusing Heat-Exchanger

Schlichting [4, pp. 460-462] and White [9, pp. 359-360] summarized the boundary-layer theory that applies to the diffusing heat-exchanger concept. Much documentation exists on the relationship between boundary-layer behavior and heat-transfer or pressure-gradients. In general, a cooled wall stabilized the flow being studied if gases were involved; contrarily, a heated wall stabilized the flow of liquids [9, p. 359]. In addition, an adverse pressure-gradient destabilized a boundary-layer and a favorable pressure-gradient stabilized it.

Cooling reduces the rate of boundary-layer growth, or momentum defect, in order for the boundary-layer to tolerate greater adverse pressure-gradients. This is understood by looking at the ratio between boundary-layer displacement (δ^*) and momentum (θ) thickness, commonly known as the shape factor, H. These terms are

defined as

$$\delta^* = \int_0^{y_e} \left(1 - \frac{\rho u}{\rho_e u_e}\right) dy, \tag{2.3}$$

$$\theta = \int_0^{y_e} \left(1 - \frac{u}{u_e}\right) \frac{\rho u}{\rho_e u_e} dy, \tag{2.4}$$

$$H = \frac{\delta^*}{\theta} \tag{2.5}$$

It is possible to see a reduction in the shape factor when cooling is expressed as a local density change. Since the boundary-layer approximation of $\frac{\partial p}{\partial y} = 0$ is assumed, the density and temperature are related by $\frac{\rho}{\rho_e} = \frac{T_e}{T}$. This is substituted into the definition for H, yielding

$$H = \frac{\int_0^{y_e} \left(1 - \frac{h_e u}{h u_e}\right) dy}{\int_0^{y_e} \left(1 - \frac{u}{u_e}\right) \frac{h_e u}{h u_e} dy}. \tag{2.6}$$

It is clear that $h_e/h > 1$ for cooling, which diminishes the integrand and likewise results in a lower shape factor. At this point, the coupling between H and θ, or reduction in momentum defect, is expressed as the well-studied T. von Kármán momentum integral equation:

$$\frac{d\theta}{dx} = \frac{C_f}{2} - (H+2)\frac{\theta}{u_e}\frac{du_e}{dx}, \tag{2.7}$$

where $C_f = \tau_w / \left(\frac{1}{2}\rho_e u_e^2\right)$ is the skin friction coefficient and u_e is the boundary-layer edge velocity. The second term relates the momentum thickness growth rate to the pressure-gradient. Due to cooling, adverse pressure-gradients become less influential as H decreases because $\frac{du_e}{dx} < 0$.

Cooling also provides increased resistance to separation by increasing the kinetic energy of the boundary-layer. This is evident by expressing the coupling between H and H^*, the kinetic energy shape parameter. H^* is known as

$$H^* = \frac{\theta^*}{\theta}, \tag{2.8}$$

where θ^* is the kinetic energy thickness defined by

$$\theta^* = \int_0^{y_e} \left(1 - \frac{u^2}{u_e^2}\right) \frac{\rho u}{\rho_e u_e}\, dy. \tag{2.9}$$

The growth rate for H^*, and its relation to H, is easily understood by the mechanical energy integral relation:

$$\frac{1}{H^*}\frac{dH^*}{dx} = \frac{2C_D}{H^*} - \frac{C_f}{2} + \left(1 - H + \frac{2H^{**}}{H^*}\right)\frac{\theta}{u_e}\frac{du_e}{dx}. \tag{2.10}$$

Undefined terms in equation (2.10) include the density thickness shape parameter, H^{**}, volume flux thickness, δ^{**}, dissipation coefficient, C_D, dissipation integral, D, and shear, τ. There definitions are summarized below:

$$H^{**} = \frac{\delta^{**}}{\theta}, \tag{2.11}$$

$$\delta^{**} = \int_0^{y_e} \left(1 - \frac{\rho}{\rho_e}\right)\frac{u}{u_e}\, dy, \tag{2.12}$$

$$C_D = \frac{D}{\rho_e u_e^3}, \tag{2.13}$$

$$D = \int_0^{y_e} \tau \frac{\partial u}{\partial y}\, dy. \tag{2.14}$$

The shape factor, H, plays a dominant role in equations (2.7) and (2.10). Via the influence of cooling, H reduces the momentum defect and increases the kinetic energy growth rates in the boundary-layer. Consequently, cooling permits greater tolerance to adverse pressure-gradients and increased resistance to separation. This is fundamental to the synergistic design concept.

In other circumstances, where transition from laminar to turbulent flow is expected, cooling inhibits transition as well. Physical reasons for these phenomenon point to the boundary-layer stability problem. Using incompressible flat plate laminar flow as a re-occurring example, the growing boundary-layer experiences 2D perturbations (unstable Tollmien-Schlichting waves) a distance x_{ind} from the plate leading edge. These disturbances evolve downstream into 3D perturbations (e.g., vor-

tex structures and turbulent spots) that essentially cause transition to a turbulent boundary-layer or flow separation at a distance x_{crit} from the leading edge.

As the local Reynolds number, Re_x, grows linearly from the leading edge, the indifference Reynolds number, $Re_{ind} = u_e x_{ind}/\nu$, identifies the onset of Tollmien-Schlichting perturbations in the laminar boundary-layer. A critical Reynolds number, $Re_{crit} = u_e x_{crit}/\nu$, defines where the transition to turbulent flow occurs.

It is well known that a cooled wall increases the indifferent Reynolds number in gases [4, p. 460]. Thus the boundary-layer experiences a delay in the creation of instabilities until further downstream, which inherently prolongs the onset of transition. In flat plate flow, where there is no pressure-gradient, this has been experimentally verified [4, p. 460]. The presence of a pressure-gradient, coupled with a cooled wall, permits an interesting flow situation. Boundary-layer response to cooling and adverse pressure-gradients is explained by looking at the velocity profile, $u(y)$, within the boundary-layer.

The velocity profile dependence on pressure-gradients is examined first. After simplifying the Navier-Stokes equations, the boundary-layer momentum equation for steady parallel flow becomes

$$u\frac{\partial u}{\partial x} + v\frac{\partial u}{\partial y} = -\frac{1}{\rho}\frac{dp}{dx} + \nu\frac{\partial^2 u}{\partial y^2}. \tag{2.15}$$

Assuming that there is no slip at the wall, where $y = 0$, means that $u(x, 0) = 0$ and $v(x, 0) = 0$. Rewriting the boundary-layer equation for conditions at the wall yields the compatibility condition at the wall

$$\mu\left(\frac{\partial^2 u}{\partial y^2}\right)_w = \frac{dp}{dx}. \tag{2.16}$$

A subscript w denotes a wall condition. Adverse pressure-gradients ($\frac{\partial p}{\partial x} > 0$) imply $\frac{\partial^2 u}{\partial y^2} > 0$ at the wall and also indicate that a point of inflection exists somewhere in the velocity profile, $u(y)$ (due to a negative second-derivative in velocity near the boundary-layer edge). This boundary-layer profile is unstable.

If a temperature gradient exists, such that the local viscosity is a function of

temperature ($\mu = \mu(T)$), then the viscous-shear term in the boundary layer equation changes to include non-constant viscosity, yielding

$$u\frac{\partial u}{\partial x} + v\frac{\partial u}{\partial y} = -\frac{1}{\rho}\frac{dp}{dx} + \nu\frac{\partial^2 u}{\partial y^2} + \frac{1}{\rho}\frac{\partial \mu}{\partial y}\frac{\partial u}{\partial y}. \tag{2.17}$$

Applying the wall conditions again, and using the chain-rule, provides a modified compatibility condition that includes the effect of temperature-gradient at the wall:

$$\mu\left(\frac{\partial^2 u}{\partial y^2}\right)_w = \frac{dp}{dx} - \frac{\partial \mu}{\partial T}\left(\frac{\partial T}{\partial y}\right)_w \left(\frac{\partial u}{\partial y}\right)_w. \tag{2.18}$$

For gases, a cold wall requires $\frac{\partial T}{\partial y} > 0$ and $\frac{\partial \mu}{\partial T} > 0$. Since $\frac{\partial u}{\partial y} > 0$ at the wall as well, it is evident that the velocity profile curvature at the wall will decrease and become more stable when the wall is cooled. This is obviously the case in the flat plate incompressible laminar boundary-layer, where no pressure-gradient exists. Destabilizing effects from adverse pressure-gradients are therefore mitigated by the stabilizing viscosity dependence on temperature when the wall is cooled.

Under these theoretical premises, a diffusing heat-exchanger can undergo greater pressure recovery with reduced viscous losses because the boundary-layer will have a lower tendency to separate or transition from laminar flow. Improved performance is also achieved through the turning vane geometry selection, as opposed to a straight-walled or conical diffuser configuration. The blade chord is inherently shorter than a conventional diffuser, which results in the development of a smaller momentum thickness, θ. With these fundamental boundary-layer concepts in mind, the numerical experimentation of a diffusing heat-exchanger is possible. The focus now rests on the numerical aspects of a diffusing heat-exchanger design.

Chapter 3

Numerical Implementation of Synergistic Design

The boundary-layer theory presented in section 2.4.1, along with the synergistic design concept itself, is numerically investigated in the following sections. A brief introduction to the computational software chosen for this study is presented, followed by an outline of the test matrix. Validation of C_p and ω sensitivities to cooling are given, in comparison to adiabatic cases, as well as an example of the boundary-layer stabilization that occurs. Using these proof-of-concept results, an exploration of the 4D design space is presented to portray the design trends that lead to optimum diffusion and cooling.

3.1 Computational Method

MISES is a computational flow solver employed to validate the synergistic design concepts expounded earlier. Prof. Mark Drela created this software at MIT for 2D inviscid/viscous flow analysis of blade rows. This software package contained a grid-generator, airfoil geometry modification routines, flow solver and plotting scripts. User input was only required for creating flow defining input files and grid initialization.

Scripts were written to drive the MISES routines and provide automatic process-

ing of a large design space. This also required plotting scripts that compiled and sorted the large amount of output data created during each sweep of design parameter changes. Of the numerous output data variables, three were selected as prime performance measures:

1. C_p, a measure of diffusion effectiveness (previously defined)

2. $H_{t_2}/H_{t_1} - 1$, a measure of total heat-exchange

3. ω, a measure of viscous losses

The viscous loss parameter was defined as

$$\omega = \frac{p_{t_2}^{isen} - p_{t_2}}{p_{t_1} - p_1}. \tag{3.1}$$

This parameter usually neglects shock-losses due to subsonic conditions in this design problem. It embodies the difference in mixed-out exit stagnation pressure to the stagnation pressure theoretically possible in isentropic flow. The stagnation pressure loss is attributed to lost work potential and denotes a non-isentropic process, where the viscous shear losses and heat-transfer lead to anisotropy.

Heat-transfer is calculated using the Reynolds Analogy. Although this method is formulated for $\partial p/\partial x = 0$, Drela has determined that errors below 20% have been noted in heat-transfer calculations of high pressure-gradient turbine blade cases. The enthalpy thickness is likewise not determined throughout the boundary-layer calculation, but rather the total thickness in the blade wake is found via integration of heat-flux over the blade surface [1, p. 17]. Finite-difference boundary-layer calculations show that an error of approximately 5%-10% is expected from MISES heat-transfer predictions when separation occurs.

The relevant input parameters included constraints on inlet Mach number, inlet Reynolds number and a wall enthalpy ratio, $H_w = h_w/h_{t_1}$. This enthalpy ratio assumed that the cooling water temperature conducted through the blade walls, leaving no thermal transient regions (besides having a constant temperature profile in the

blade walls). Furthermore, the steady-state distribution of wall temperature across the blade was assumed constant.

3.2 Numerical Test Matrix

The diffusing heat-exchanger design space was limited to incorporate geometry specifications that could yield reasonable results (e.g., reasonable losses). Wilson outlined that blade-row solidity, $\sigma = chord/pitch$, variations contain an optimum value for minimal total pressure loss [10, p. 242]. He also explained how selecting the blade setting angle, θ, was not far removed from the realm of art to that of science [10, p. 250]. With these general concepts in mind, the design space was limited to the following parameter ranges:

1. Pitch (s) ϵ [0.1, ... , 1]
2. Chord (c) ϵ [0.2, ... , 3.25]
3. Setting angle (θ) ϵ [-24, ... , 24] (degrees)
4. H_w ϵ [0.2, ... , 1]

Besides these parameters, an estimate of channel boundary-layer blockage was selected using the flat-plate Blasius displacement thickness definition for laminar flow:

$$\frac{\delta^*}{s} = 2\frac{1}{s}\frac{5c}{\sqrt{Re_c}} = \frac{c}{s}\frac{10}{\sqrt{Re_c}}. \tag{3.2}$$

This provided an indication of how thermal energy was extracted from the mean flow. Boundary-layers above and below the blade surface contributed to half the blockage, thereby requiring the factor of 2. By assuming that the thermal boundary-layers developed an enthalpy thickness similar in height to the displacement thickness, equation (3.2) implied that remaining regions of core flow resulted in lost thermal energy. As $d\delta/ds \rightarrow 1$, $H_{t_2}/H_{t_1} - 1 \rightarrow -1$, and fully-developed channel flow would ensue without cooling.

A diffusing blade row was defined using a thin cambered airfoil with ample flow turning (approximately 45^o). The diffusing heat-exchanger was proposed as an annular design which contained a cross-section similar to that of a turbomachine blade row. Figure 3-1 shows a cross-section with added geometry definitions. This enabled a 2D viscous calculation simulation rather than employing a 3D internal flow prediction for conceptual evaluation. Limitations inherent in a 2D code, though, included a loss of information regarding swirl, secondary-flows and uneven cooling around the annulus circumference (which would yield uneven circumferential pressure-gradients and induce cross-flow). Non-uniform cooling was neglected, however, by assuming if the coolant flow rate was sufficient to maintain a constant wall temperature. These higher-order effects needed evaluation in a more detailed analysis.

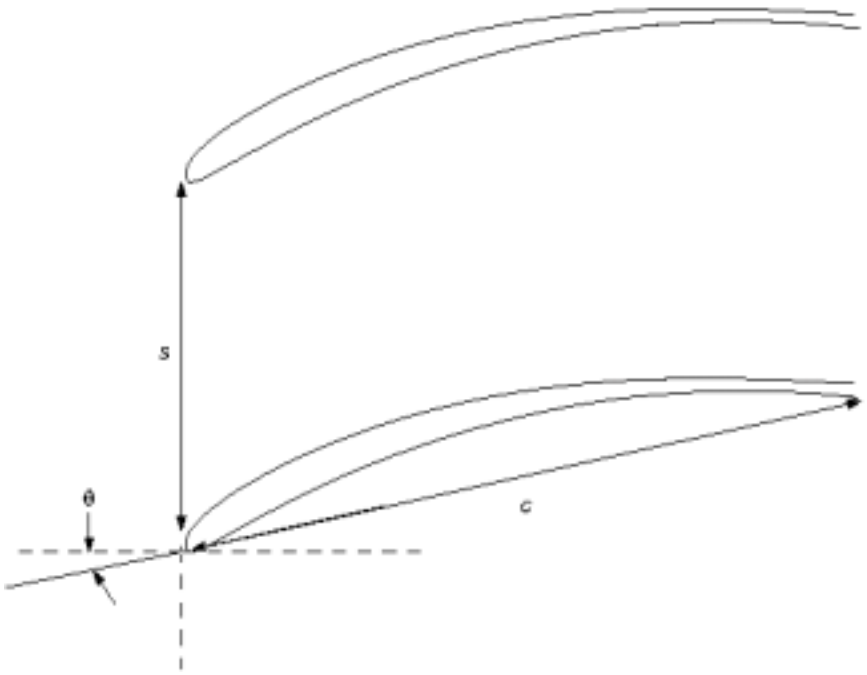

Figure 3-1: Annular design cross-section with standard geometry definitions.

Initial flow conditions were selected at $M_1 = 0.25$ and $Re = 4000$, a baseline Reynolds number. The inlet flow was anticipated as subsonic and low Reynolds numbers were likewise of interest. In the range of possible H_w values, $H_w = 0.5$ was used to test the changes in pitch, chord or setting angle.

The design space outlined above was studied using the automatic MISES driver scripts. External scripts modified the blade row geometry and collected MISES output data while the internal MISES codes provided the flow solutions. Each combination of solidity, setting angle, and wall enthalpy ratio was used to provide surface plots of C_p, $H_{t_2}/H_{t_1} - 1$ and ω performance trends. Example solution grids created in MISES were displayed in figure 3-2 and numerical results obtained detailed interpretations in the following section.

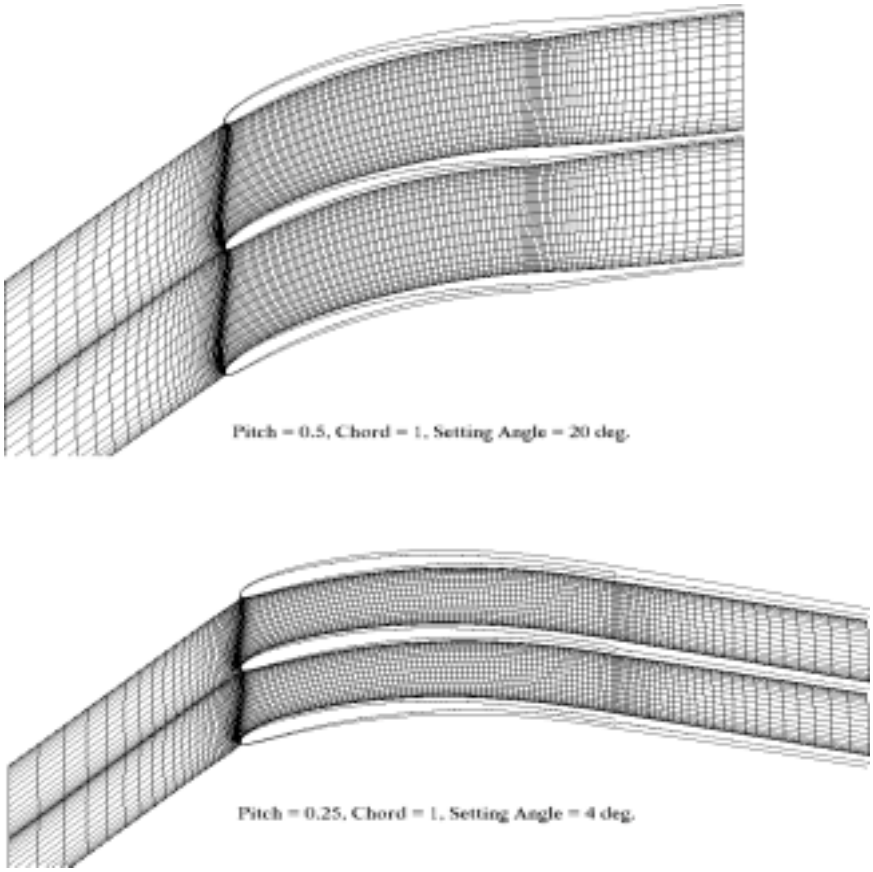

Figure 3-2: Example solution grids generated by MISES.

3.3 Numerical Concept Validation

Two objectives needed validation in the trials between adiabatic and non-adiabatic flows:

1. C_p improvement

2. ω reduction

A third objective included minimizing $H_{t_2}/H_{t_1} - 1$ (this term is negative for cooled flow) to verify how much steam production was possible. These performance values were compiled for various pitch, chord, setting angle and wall enthalpy ratios. The blade geometry was defined as portrayed in figure 3-1 during all numerical investigations.

3.3.1 Sensitivity of C_p to H_w

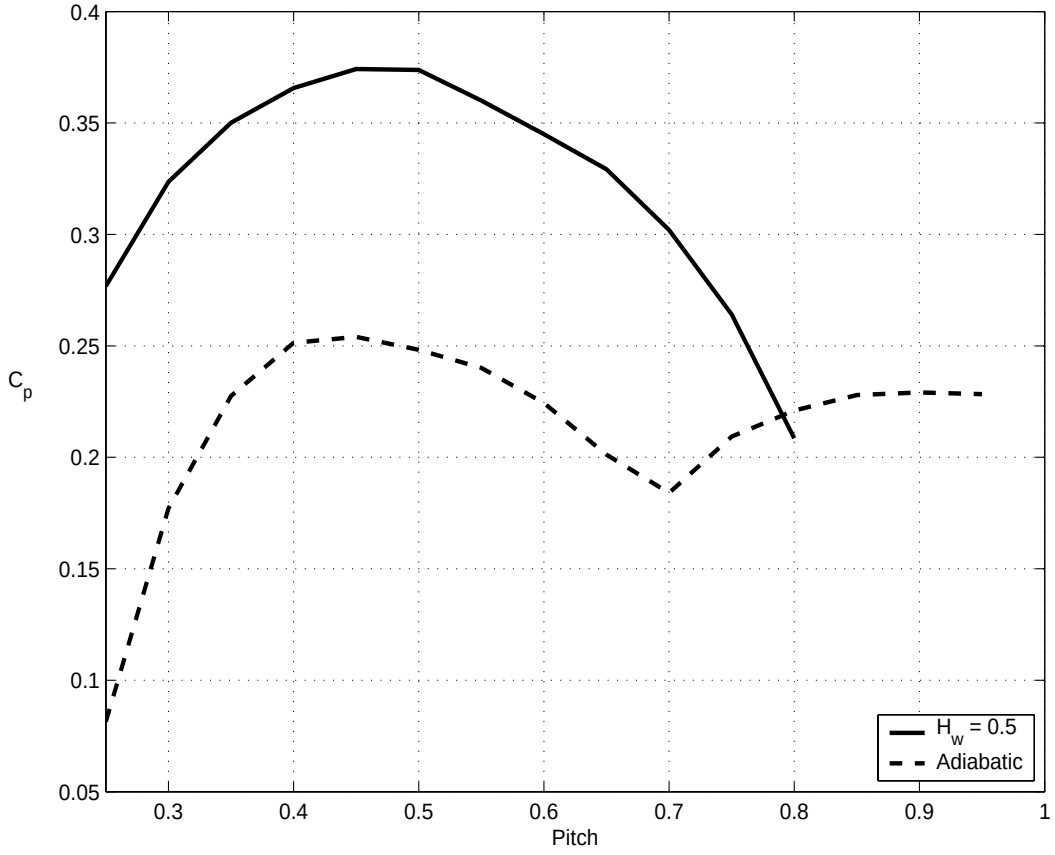

Figure 3-3: The C_p sensitivity to pitch changes is considered for adiabatic and non-adiabatic flow.

Figure 3-3 depicts the sensitivity of C_p to variations in pitch with and without cooling (adiabatic case). Setting angle and chord were held constant at 12 degrees

and 1, respectively. A clear improvement in C_p existed due to heat-transfer. The optimum pitch shifted slightly due to heat-exchange; yet the optimum C_p value was improved by approximately 47%.

The adiabatic case provides an interesting result in the sense of two local maximums. Beyond a pitch value of 0.7, the boundary-layer flow appears to form a separation bubble that permits further pressure-recovery. A slight improvement in diffusion performance is seen, yet ultimately falls short of the global maximum found at the pitch value of 0.45. It is also conceivable that the non-adiabatic case stabilized the boundary-layer sufficiently to negate the opportunity of a separation bubble to form.

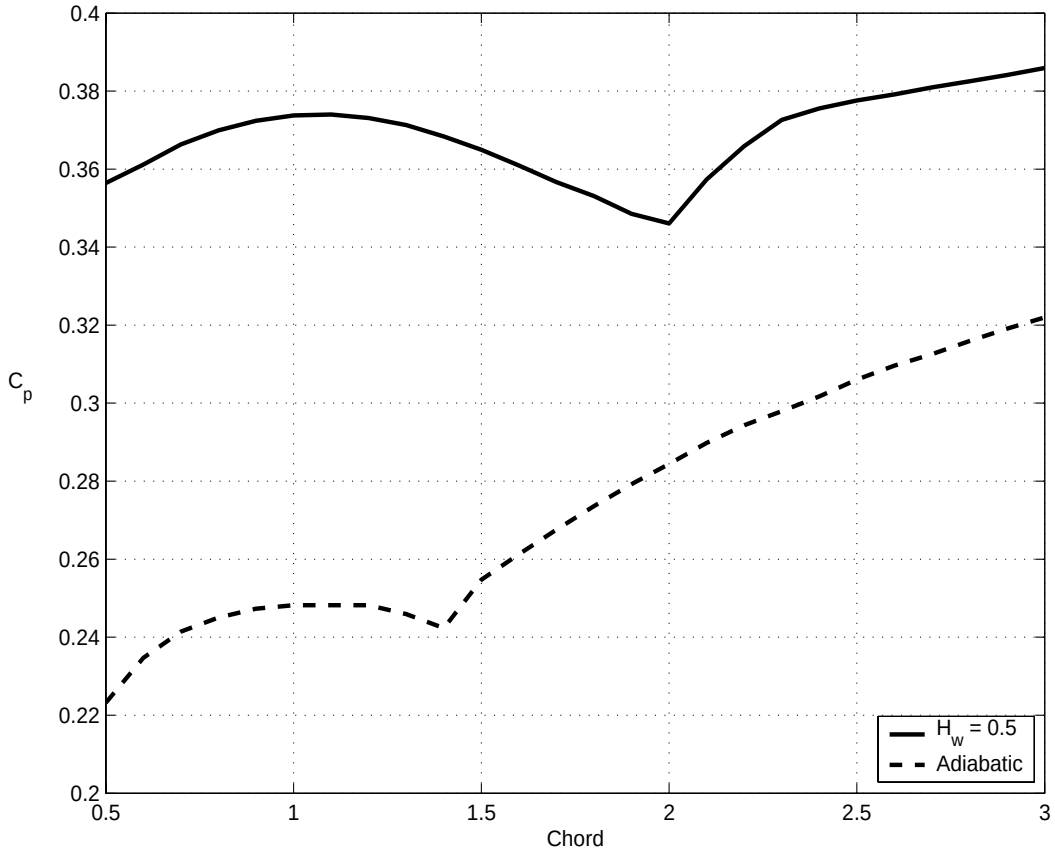

Figure 3-4: The C_p sensitivity to chord changes is considered for adiabatic and non-adiabatic flow.

Figure 3-4 provides a similar look at the effect of heat-exchange on pressure-recovery for different chord scalings (Reynolds number variations). Setting angle and

pitch are held constant at 12 degrees and 0.5, respectively. Another 48% improvement in pressure-recovery performance is permitted through heat-exchange at lower chord scales. A local maximum occurs near a chord value of 1; however, a much better C_p is apparent for higher chord scaling factors. Essentially, a higher Reynolds number results from larger chord scales and implies a greater influence of inertial over viscous forces. This stabilizing effect is coupled by the flow cooling mechanisms to allow better diffusion at higher chord values. The limit of large chord approaches the common tunnel diffuser configuration, which is already known to provide the highest C_p values for small wall expansion angles.

The discontinuity at $c = 2$ is another demonstration of a separation bubble emerging in the boundary-layer. A proof of separation bubble existence is found in figure 3-5, where $c = 3$, because the C_p blade distribution shows a discontinuity as well. The adiabatic and non-adiabatic C_p distributions are plotted to also show how heat-exchange delayed the onset of separation further aft on the blade, which implies an increase in Re_{ind}.

Finally, the effect of cooling on pressure-recovery is observed for changing setting angles in figure 3-6. An optimum C_p value is found near a setting angle of 14 degrees. Fortunately, the best C_p is not sensitive to small variations in setting angle near the optimum. The heat-exchange allows a 36% increase in pressure-recovery over the adiabatic diffuser.

3.3.2 Sensitivity of H and $\left(\partial^2 u/\partial y^2\right)_w$ to H_w

It is self-evident that the synergistic design of a diffusing heat-exchanger is beneficial for diffusion based on the results above. The variation in boundary-layer behavior due to heat-exchange was also documented. Using the blade geometry $s = 0.5$, $c = 1.0$ and $\theta = 12^o$, the change in boundary-layer pressure and H distribution were sought between the adiabatic and $H_w = 0.5$ cases. Figure 3-7 depicts the changing pressure distribution and figure 3-8 shows the variation in boundary-layer shape factor, H. The adiabatic shape factor distribution demonstrates separated flow. The separated boundary-layer has sufficient displacement thickness to decrease the mean flow area

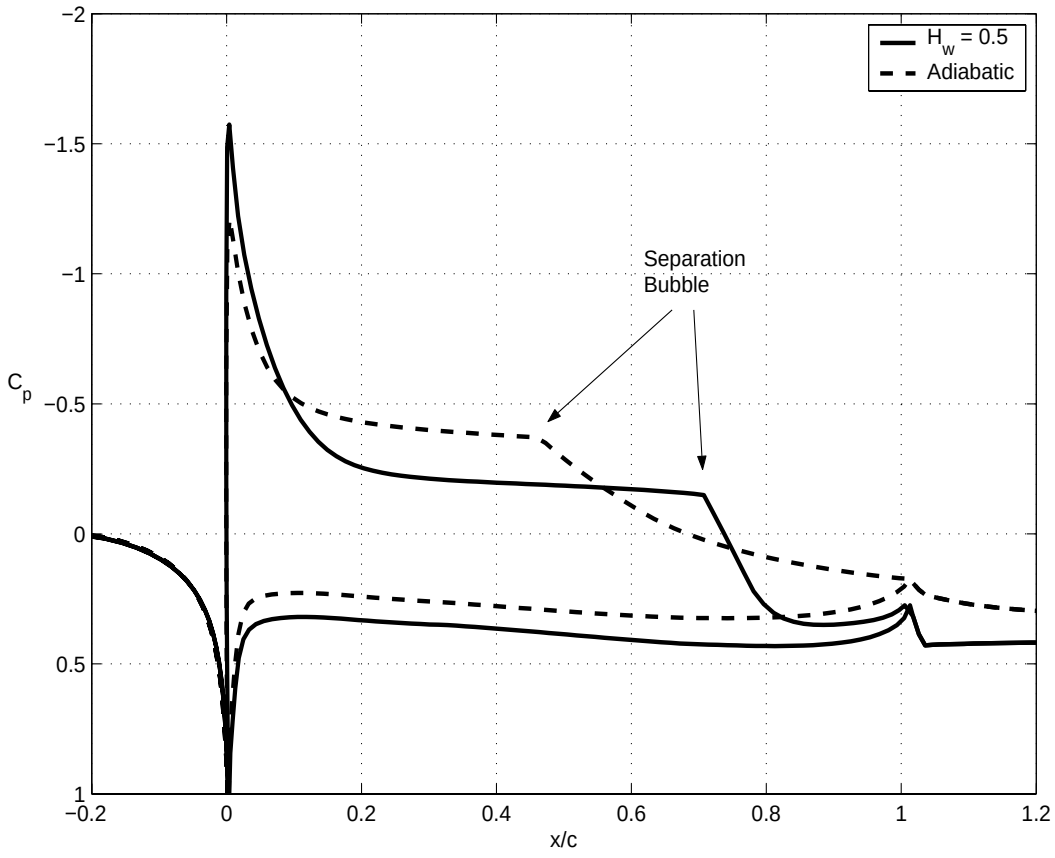

Figure 3-5: Evidence of a separation bubble, in addition to the delay of separation, resulting from heat-exchange.

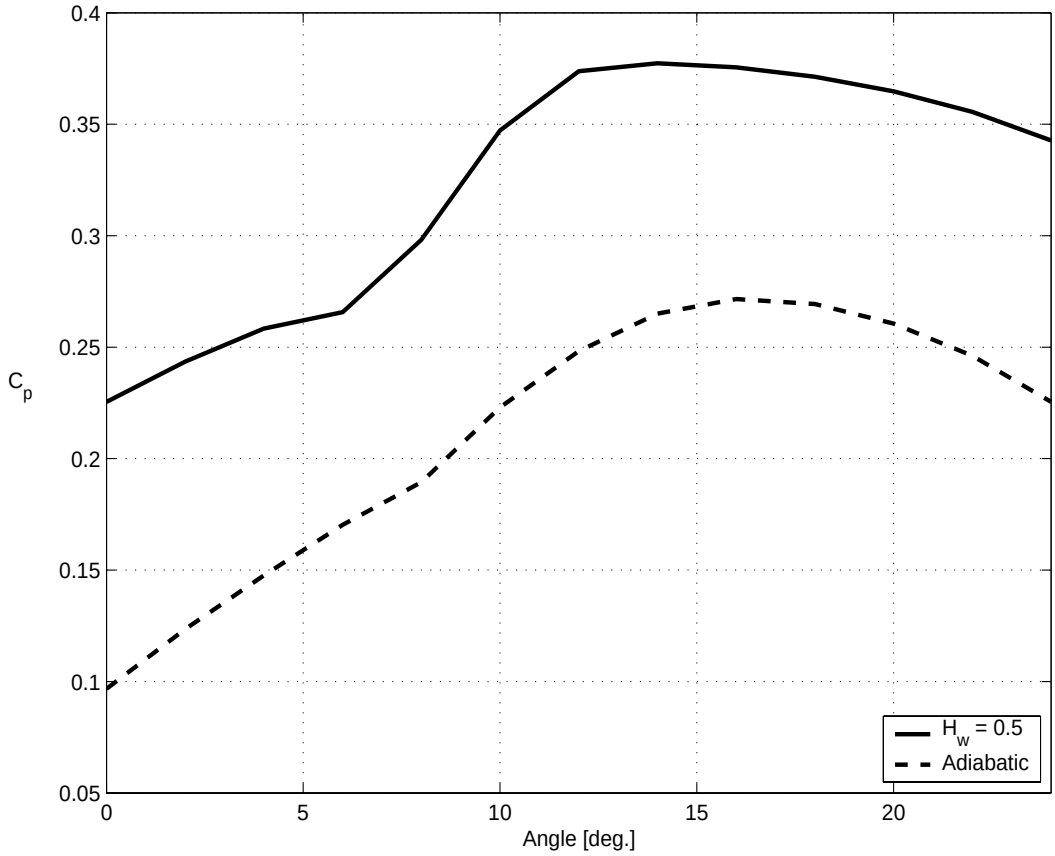

Figure 3-6: The C_p sensitivity to setting angle changes is considered for adiabatic and non-adiabatic flow.

and negate diffusion, which is illustrated by the negative C_p distribution in figure 3-7. The heat-transfer case permits non-separated flow that results in positive C_p at the trailing edge.

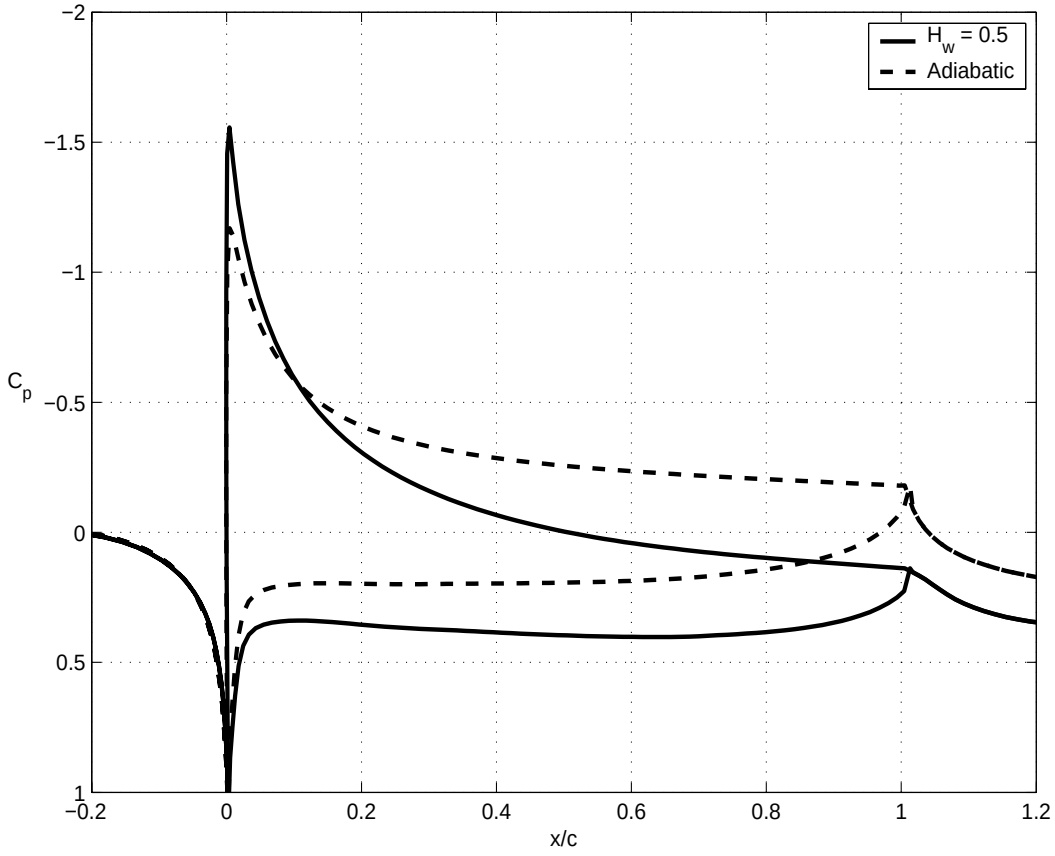

Figure 3-7: The influence of heat-transfer on the C_p boundary-layer distribution.

In addition to the bulk boundary-layer parameters C_p and H, the variation in velocity profile due to heat-exchange provides insight on boundary-layer stability. Figure 3-9 depicts the boundary-layer velocity profiles for non-adiabatic and adiabatic flow. The top-surface velocity profile curvature is positive near the wall in the adiabatic case (separation) and negative for the non-adiabatic case (no separation). This is further indication of boundary-layer stabilization as a result of flow cooling.

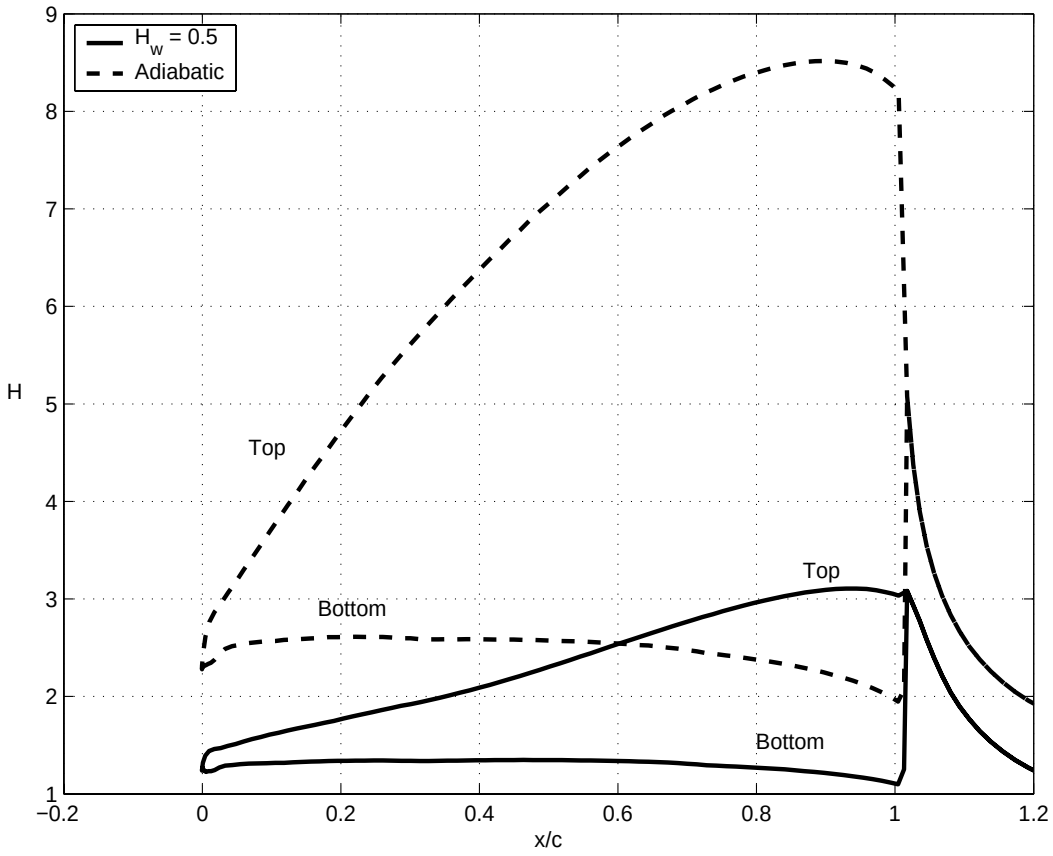

Figure 3-8: The influence of heat-transfer on the shape factor distribution, H, in the boundary-layer.

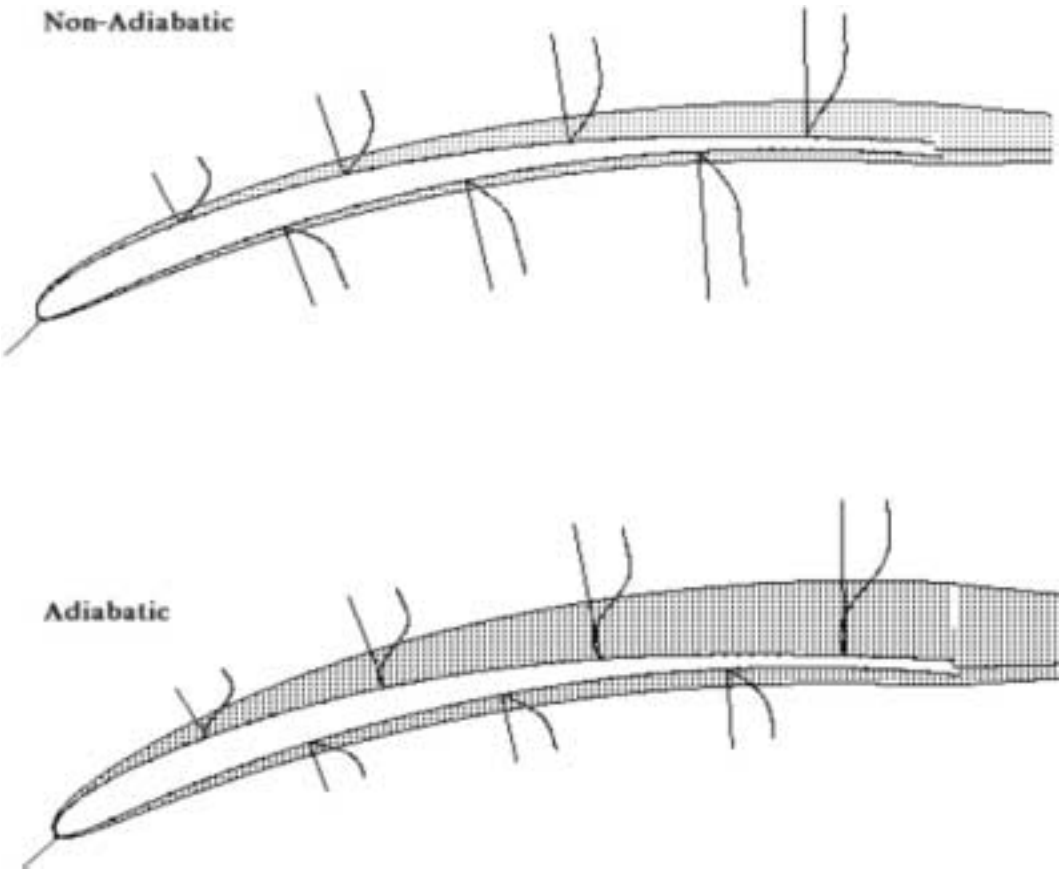

Figure 3-9: The effect of cooling on the velocity profile curvature within the boundary-layer.

3.3.3 Sensitivity of ω to H_w

The benefits seen in C_p performance were complemented by improvements in viscous losses as a consequence of non-adiabatic flow. When pitch, chord or setting angles were set constant, their values were $s = 0.5$, $c = 1$ and $\theta = 12$ degrees, respectively. These values were equivalent in generating the C_p test results previously shown.

Figure 3-10 shows a minimum non-adiabatic ($H_w = 0.5$) viscous loss, attributed to a pitch value near 0.5, that is approximately 43% less than the adiabatic minimum. This plot appears as an inverted version of figure 3-3 because the best C_p is only possible during a flow state that minimizes viscous loss. The adiabatic ω curve also contains the presence of a boundary-layer separation bubble, as mentioned above for figure 3-3.

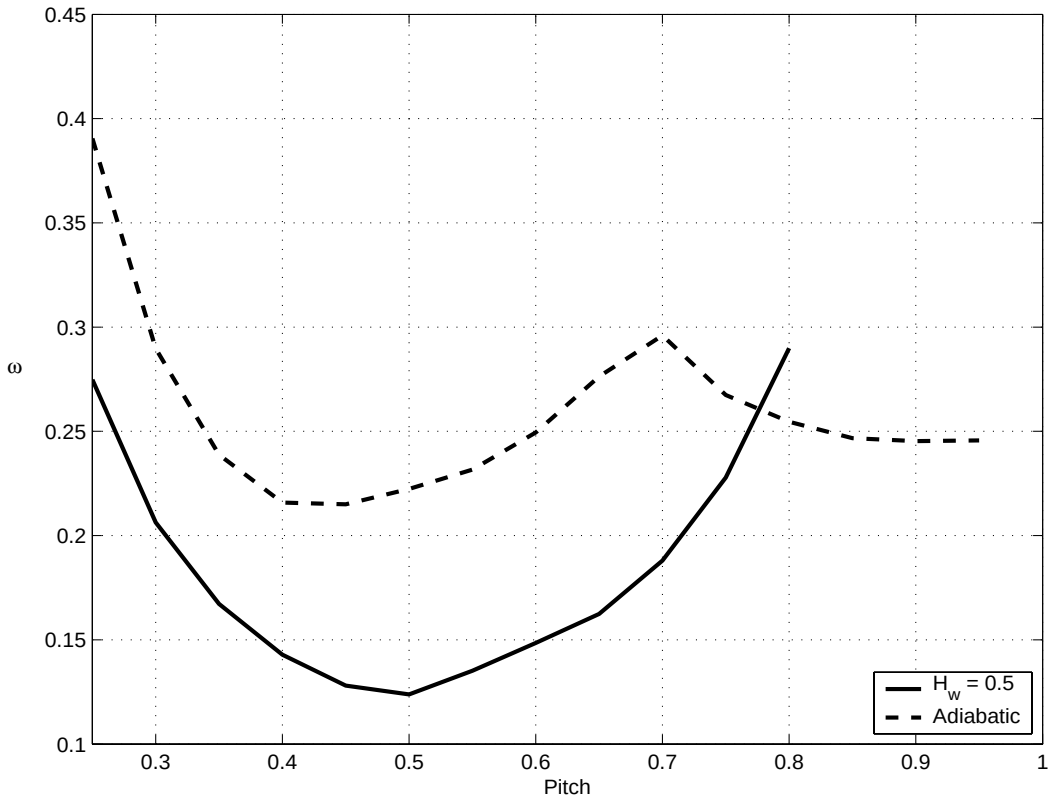

Figure 3-10: The change in viscous losses, ω, due to heat-exchange at different pitch values.

Figure 3-11 depicts a trend that parallels that of figure 3-4, where large chord values create a separation bubble and heat-transfer provides even lower viscous losses. The non-adiabatic case shows a 32% reduction in loss over the adiabatic case at $c = 3$.

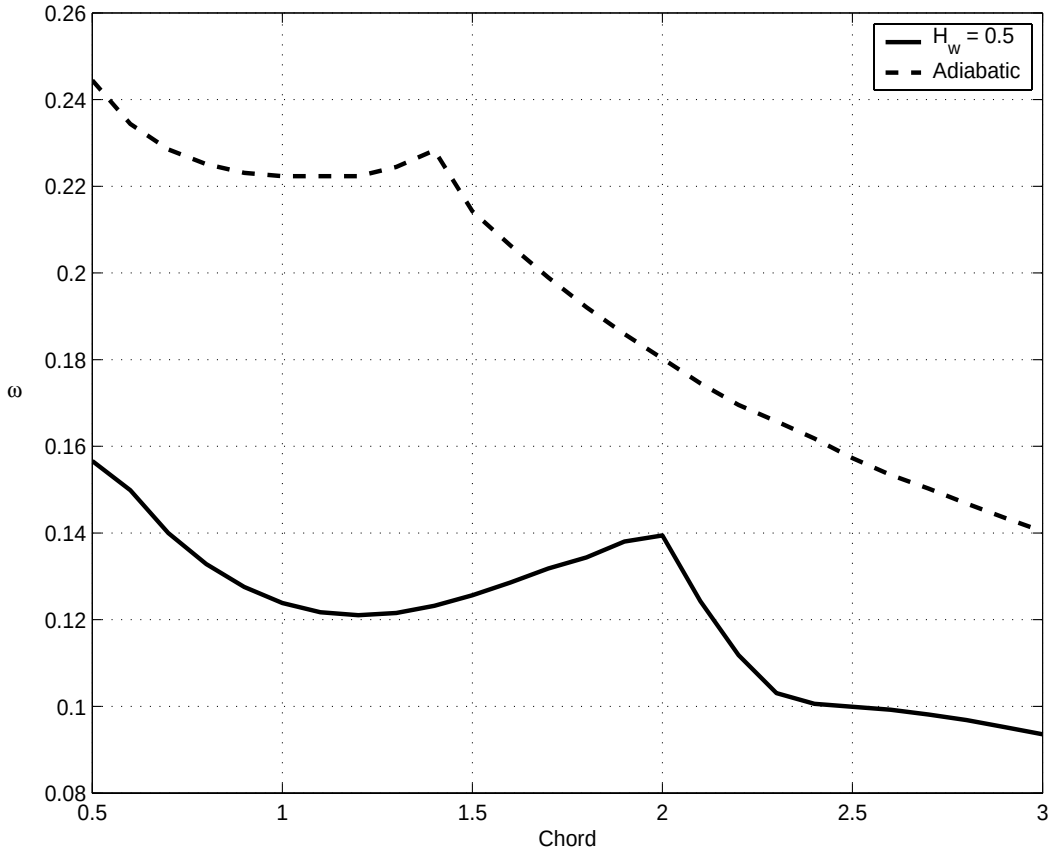

Figure 3-11: The change in viscous losses, ω, due to heat-exchange at different chord values.

A relatively flat minimum is found in figure 3-12, where small changes in the setting angle near 15 degrees provide about 37% less viscous loss in the non-adiabatic case than in the adiabatic case. This plot has similar connotations to that found in figure 3-6, where the best C_p also occurred near 15 degrees.

3.4 4D Design Space Exploration

With the numerical validation of the boundary-layer theory complete, in regards to the synergistic design concepts, an exploration of the diffusing heat-exchanger design

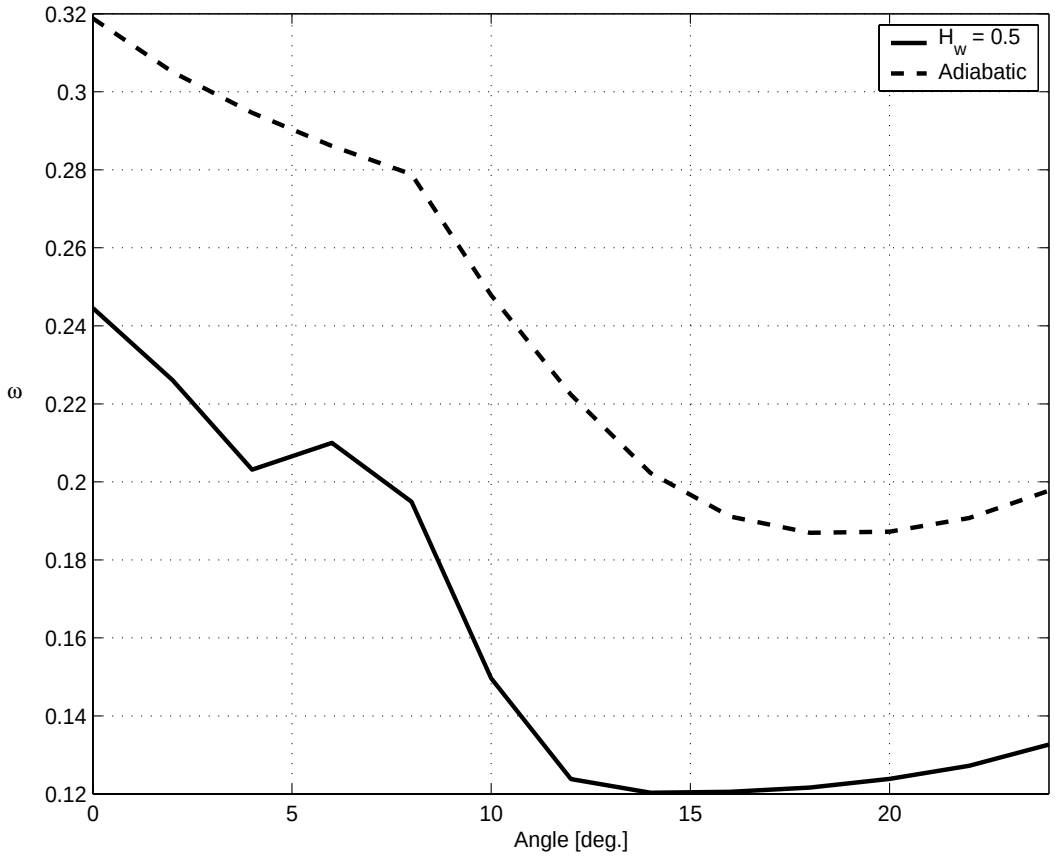

Figure 3-12: The change in viscous losses, ω, due to heat-exchange at different setting angles.

space was now possible. Four independent parameters were considered: pitch, s, chord (Reynolds number scaling), c, setting angle, θ, and wall-enthalpy ratio, H_w. This 4D design space did not provide an intuitive basis for determining the configuration that yielded an optimum C_p, ω or $H_{t_2}/H_{t_1} - 1$. In the event that only one parameter was varied, an intuitive design sense could be utilized. However, any combined variation of geometry and cooling could demonstrate unforeseen sensitivity couplings.

Initially, the numerical test matrix was used to generate performance plots at constant $H_w = 0.5$. A slice of the 4D design space yielded the 3D surfaces presented in figure 3-13 and showed the extent of possible heat-transfer across the entire geometry parameter map. Surfaces of constant pitch and chord were plotted to show their distinct effect on heat-transfer. Heat-transfer did not change much for different setting-angles. However, the heat-transfer slope was steeper for smaller pitch and chord values.

Slices of the 4D design space that measure C_p and ω were also constructed in figures 3-14 and 3-15, respectively, at $H_w = 0.5$. These 3D component surfaces were plotted separately at constant pitch and chord values due to excessive clutter. Figure 3-14 shows an increase in C_p as both pitch and chord are increased; likewise, figure 3-15 shows a decrease in viscous losses for increasing pitch and chord values. Discontinuous ridges or valleys show the onset of separation bubble formation, as seen in the 2D design map slices viewed previously. Any missing surface points resulted from non-converged solutions.

In addition to the effect of geometry changes, an understanding of the cooling effect at different wall-enthalpy ratios was also studied. These investigations provided a sense of any coupling between geometric and wall temperature changes. Slices of the 4D design space were again used to identify performance sensitivities to such coupling.

3.4.1 Performance Sensitivity to Pitch, s, and H_w

The surface plot for various pitch and H_w values appears in figure 3-16 for $c = 1$ and $\theta = 12^o$. The adiabatic line occurs at $H_w = 1$. Distinctive features on the surface

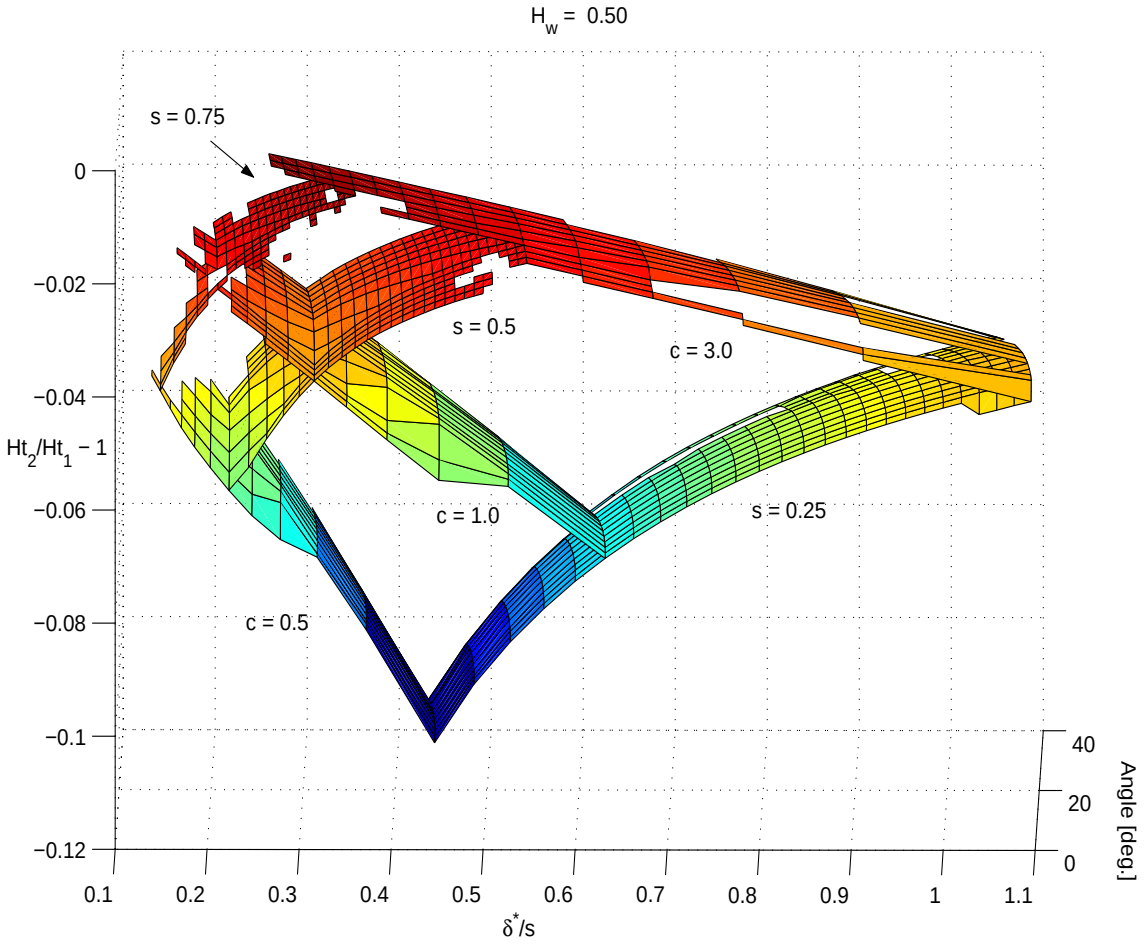

Figure 3-13: A slice of the 4D design space, revealing component 3D surfaces, for heat-transfer performance across the full geometry parameter map.

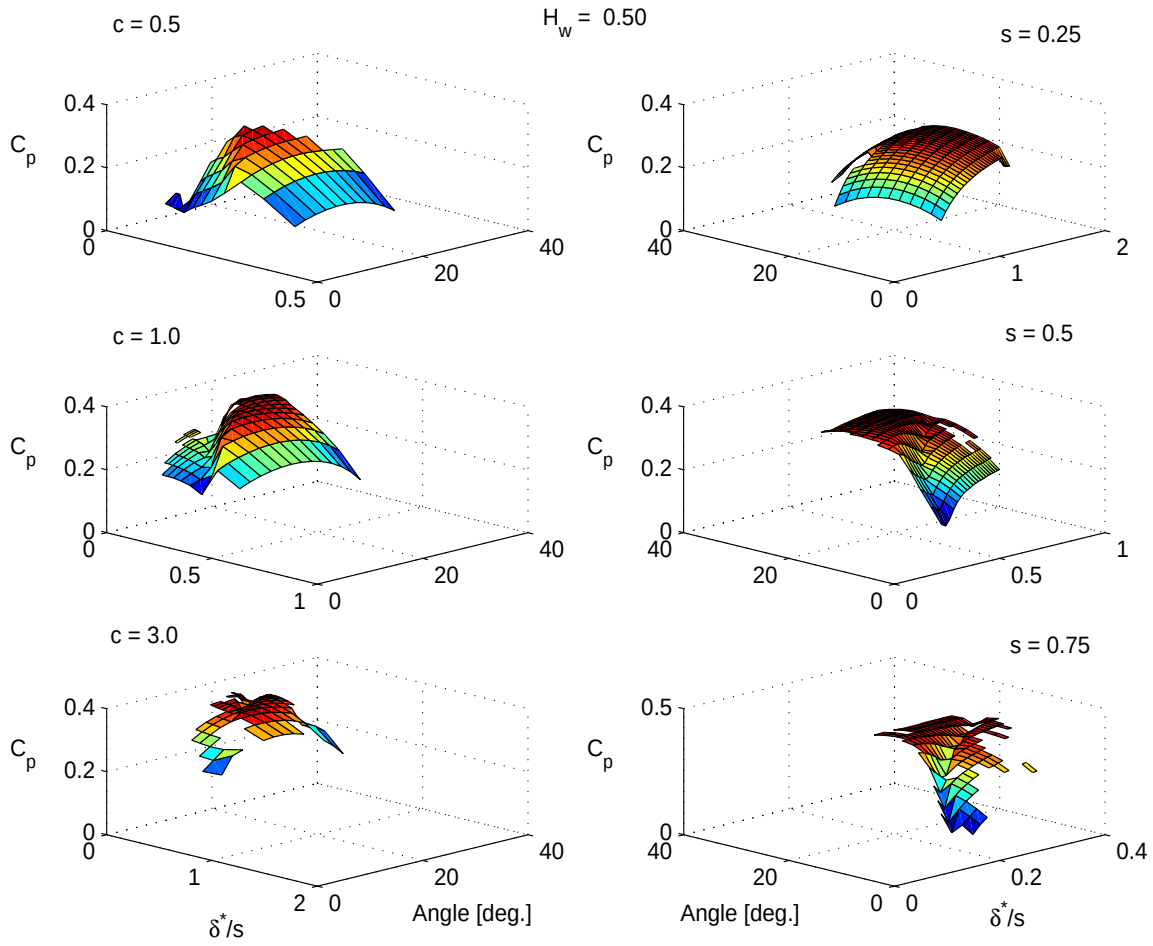

Figure 3-14: A slice of the 4D design space, revealing component 3D surfaces, for diffusion performance across the full geometry parameter map.

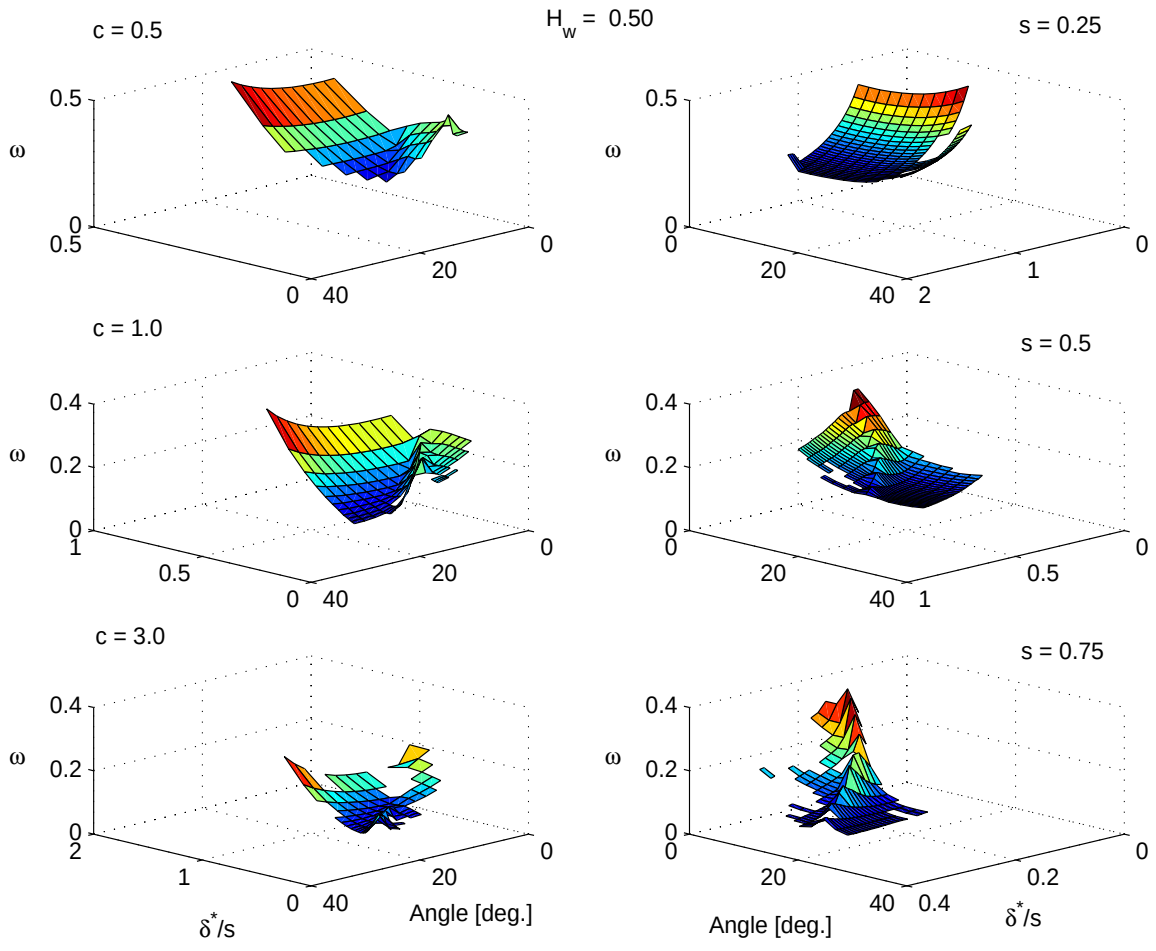

Figure 3-15: A slice of the 4D design space, revealing component 3D surfaces, for viscous loss performance across the full geometry parameter map.

plot include a valley region attributed to the onset of separation bubble formation. C_p appears to change linearly with H_w for most pitch values, where a low H_w ratio encourages greater diffusion. It is also obvious that for any H_w ratio, set by the coolant temperature, the best C_p is found with proper pitch selection; yet C_p is generally more sensitive to changes in H_w.

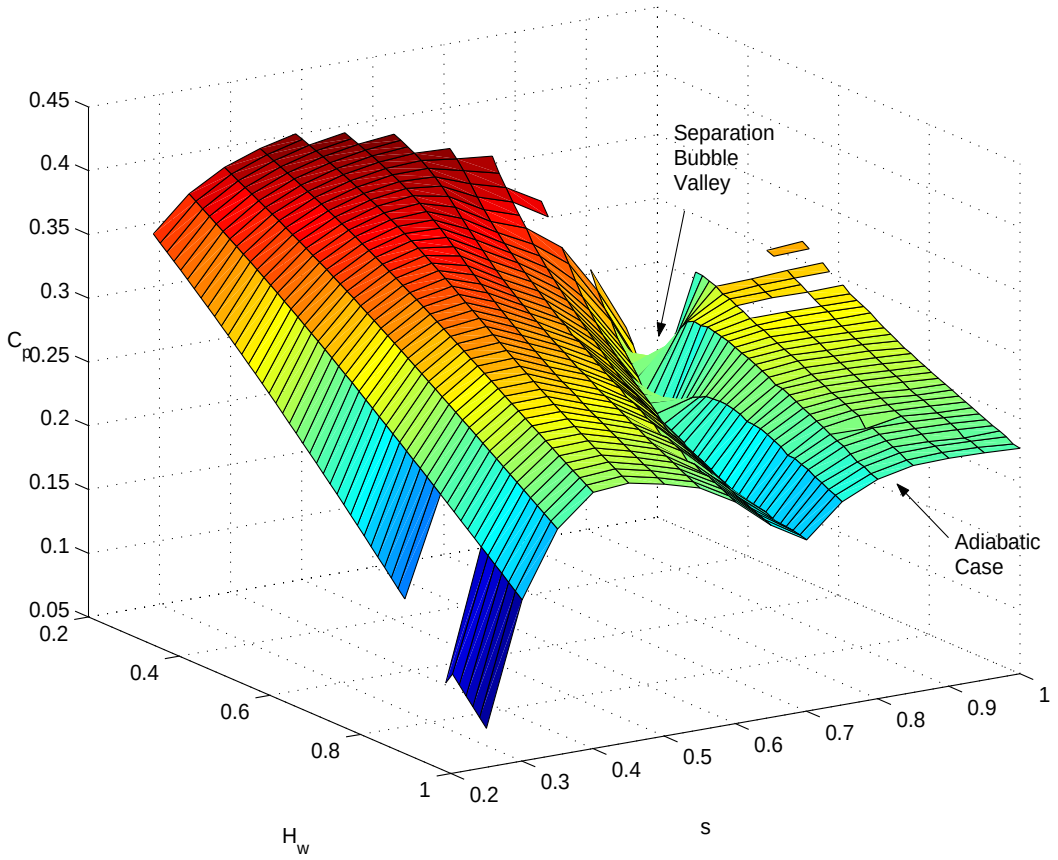

Figure 3-16: Diffusion performance due to changing H_w and pitch.

Figure 3-17 provides a plot of viscous loss performance for various H_w and pitch values at $c = 1$ and $\theta = 12^o$. The adiabatic case shows the highest possible loss, as expected, and a ridge exists that identifies the onset of a separation bubble. When pitch lies within the domain that creates local ω minimums, it appears that ω depends mostly on H_w.

Lastly, figure 3-18 depicts the change in total enthalpy at different pitch and H_w values. Heat-exchange becomes much more feasible at low pitch values and low H_w

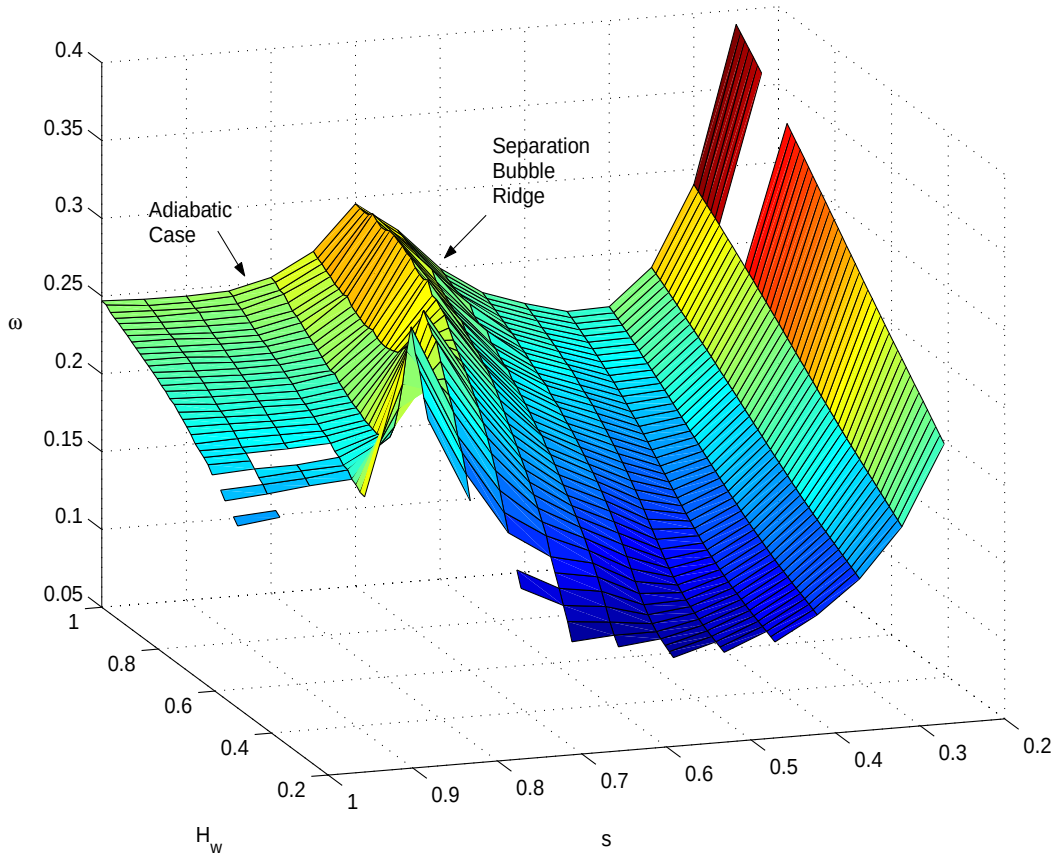

Figure 3-17: Viscous loss performance due to changing H_w and pitch.

ratios. This reflects the notion that a greater fraction of the mean flow is penetrated by the thermal boundary-layer. Lower wall temperature exacerbates this effect. In addition, the heat-transfer does not undergo any improvements due to a separation bubble formation. Hence, the lack of ridges or valleys in the surface plot indicates that the thermal boundary-layer growth is indifferent to the transition modes in the viscous boundary-layer. Although, in reality, more heat-transfer is possible in a turbulent rather than laminar boundary-layer, due to greater energy exchange between fluid eddies, the MISES code does not model these effects well through the Reynolds analogy. The skin-friction coefficient, C_f, essentially does not change much due to the separation bubble. A solution of the energy equation in the boundary-layer is necessary to model these higher-order effects.

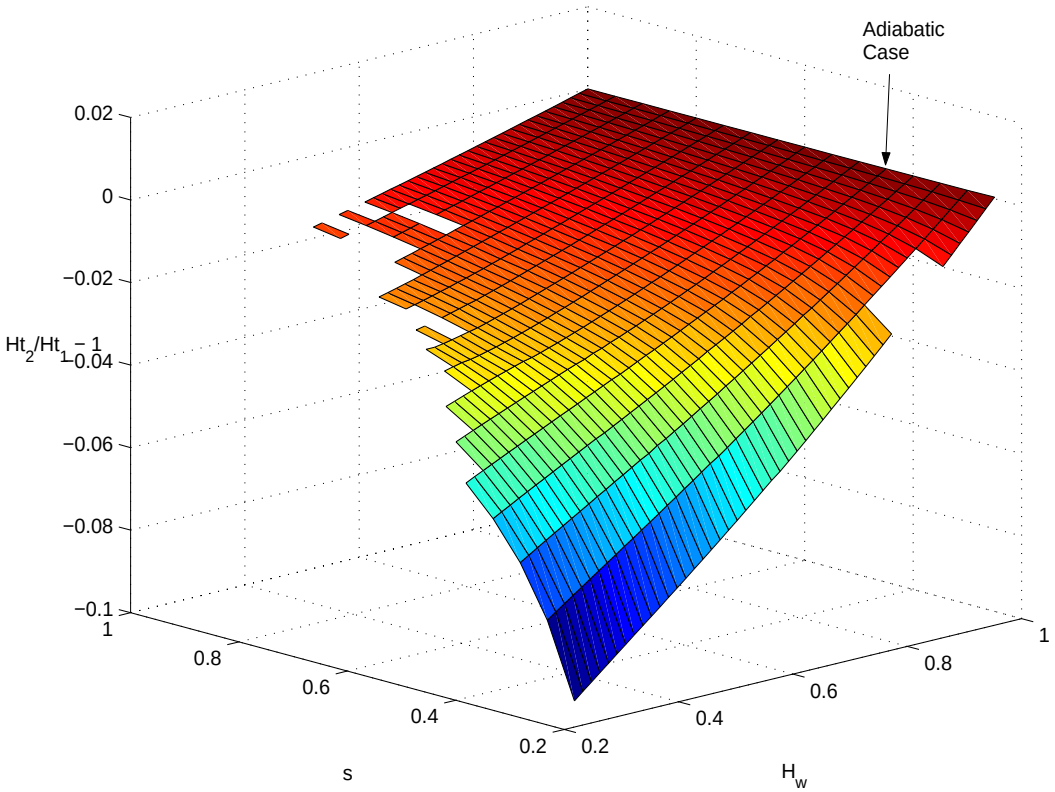

Figure 3-18: Heat-transfer performance due to changing H_w and pitch.

3.4.2 Performance Sensitivity to Chord, c, and H_w

A review of performance sensitivities to changes in chord, or Reynolds number scaling, and H_w is presented next. Pitch was fixed at $s = 0.5$ and setting angle maintained at $\theta = 12^o$ in these numerical experiments. Figure 3-19 shows the C_p performance. The surface valley representing the onset of a separation bubble moves further aft with increasing chord and decreasing H_w, meaning that the location x_{ind} moves Re_{ind} aft on the blade as a result of greater boundary-layer stabilization. If x_{ind} is greater than c, the chord length, then the boundary-layer remained laminar on the entire blade upper-surface.

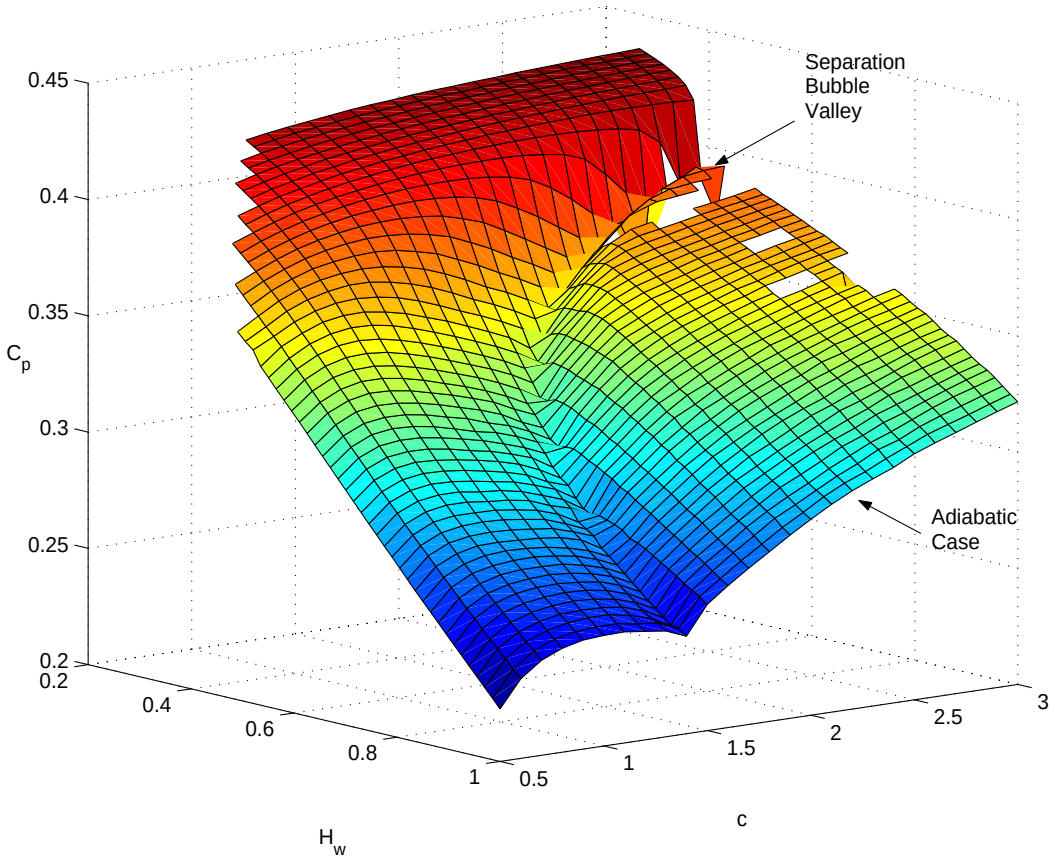

Figure 3-19: Diffusion performance due to changing H_w and chord.

Figure 3-20 depicts viscous loss versus H_w and chord changes. Even as improved C_p is obtained via larger chord scaling, the same geometry increase accomplishes a reduction in losses. Thus, the separation bubble ridge has a similar space-curve

to that found in figure 3-19. Chord lengthening also appears to have the greatest influence on both C_p and ω beyond the separation ridge.

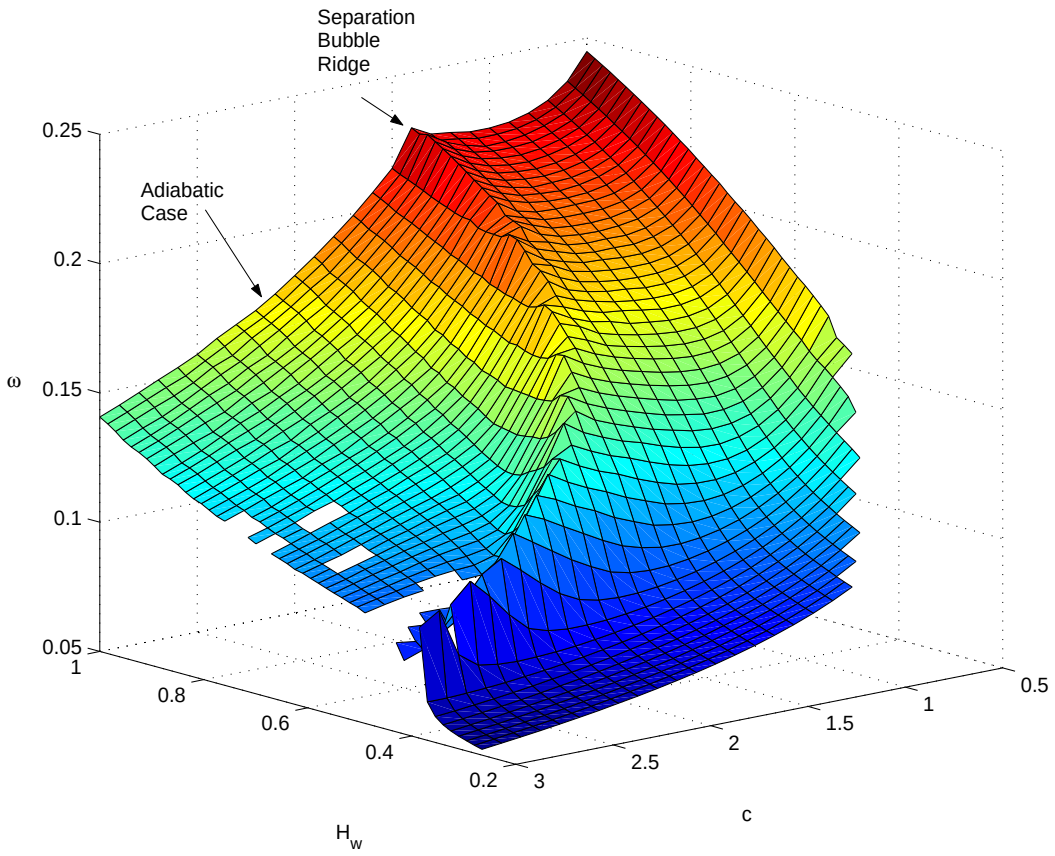

Figure 3-20: Viscous loss performance due to changing H_w and chord.

Furthermore, the heat-transfer possibilities at different H_w and chord values are plotted in figure 3-21. Heat-exchange depends linearly on H_w, since total enthalpy changes vary linearly with static enthalpy. Yet there is a steep improvement in heat-transfer at low chord. For constant Prandtl number flows, as assumed in these numerical tests, the Stanton number is inversely proportional to Reynolds number ($St_c \propto Re_c^{-\alpha}$ and $St_c \propto U$, where α is a constant depending on laminar or turbulent flow and U is the heat-transfer coefficient). Thus, a decrease in chord reduces the chord-based Reynolds and increases the Stanton number, which likewise increases the blade heat-transfer coefficient.

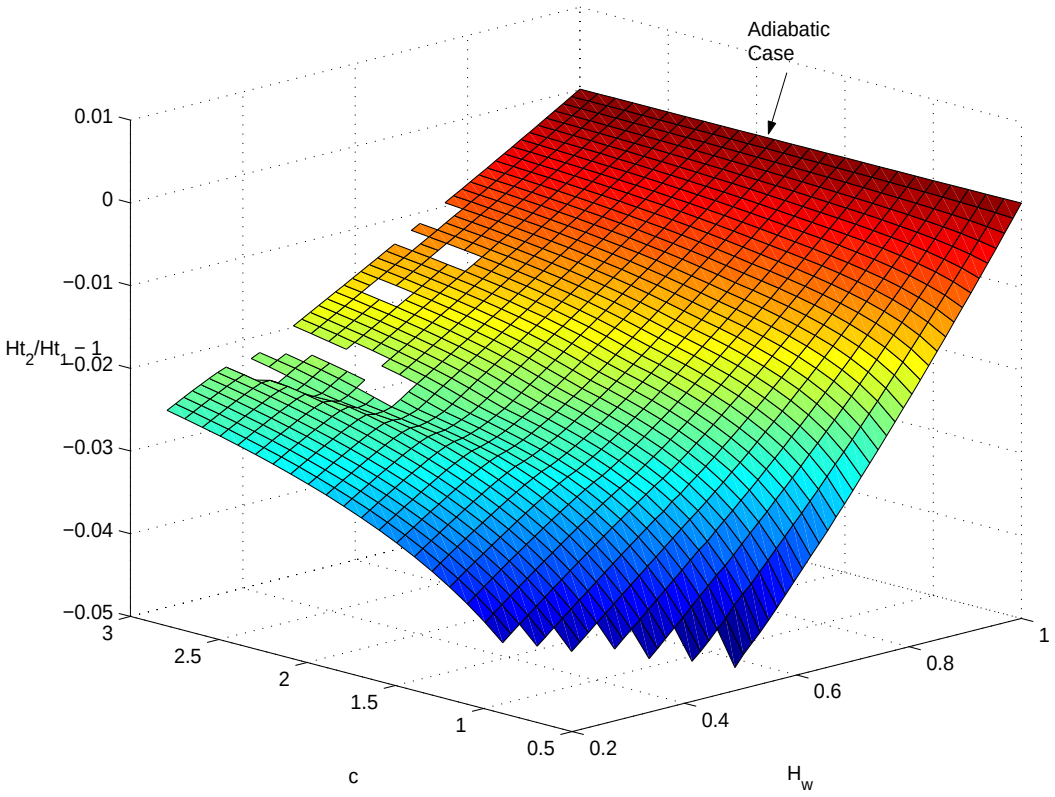

Figure 3-21: Heat-transfer performance due to changing H_w and chord.

3.4.3 Performance Sensitivity to Setting Angle, θ, and H_w

The setting angle was the final geometry parameter varied at different H_w. In figure 3-22 it is clear that C_p was influenced more by the setting angle than H_w. A ridge denoting the onset of a separation bubble was also apparent. Essentially, higher C_p values at lower setting angles were possible due to lower H_w ratios, in which added boundary-layer stabilization permitted increased flow turning.

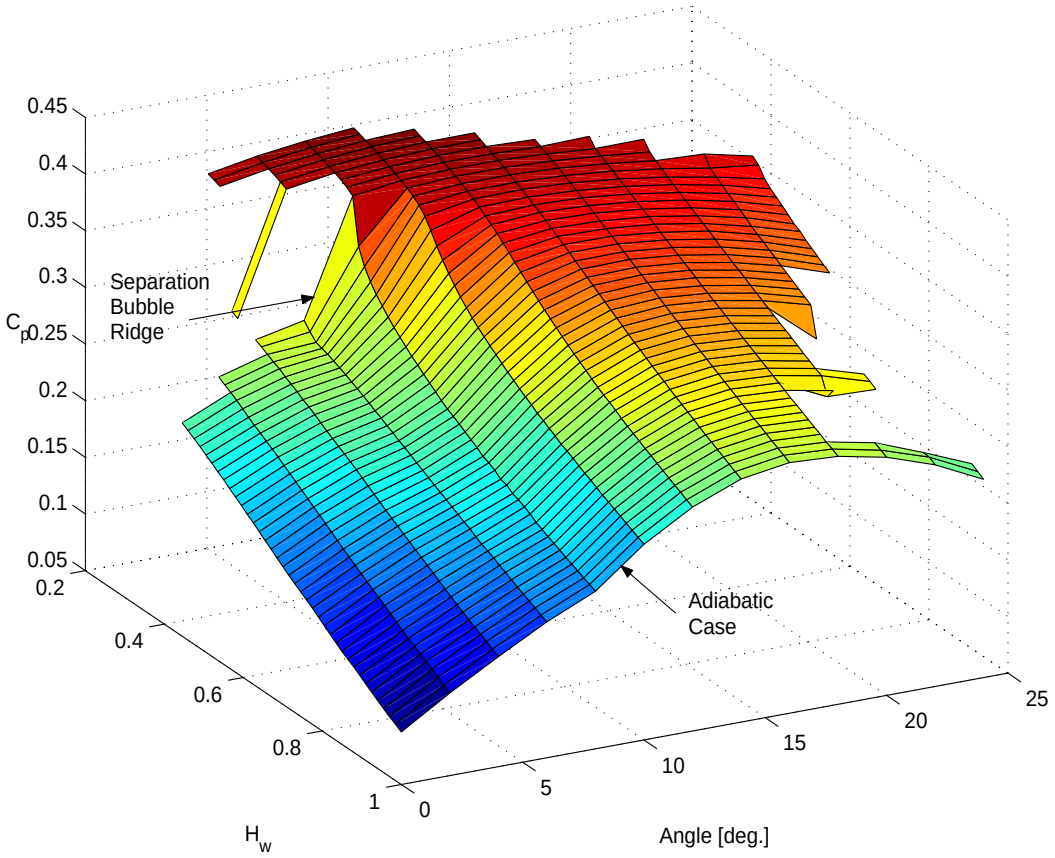

Figure 3-22: Diffusion performance due to changing H_w and setting angle.

Figure 3-23 provides a similar outlook to that seen in the C_p performance plot of figure 3-22. The lowest points of viscous loss correspond to the highest points of C_p. At the lowest H_w ratios, there is a broad setting angle range that provides low viscous loss, meaning that the boundary-layer is sufficiently stable for a wide setting angle tolerance.

The setting angle has a small influence on heat-transfer, as is the case in figure

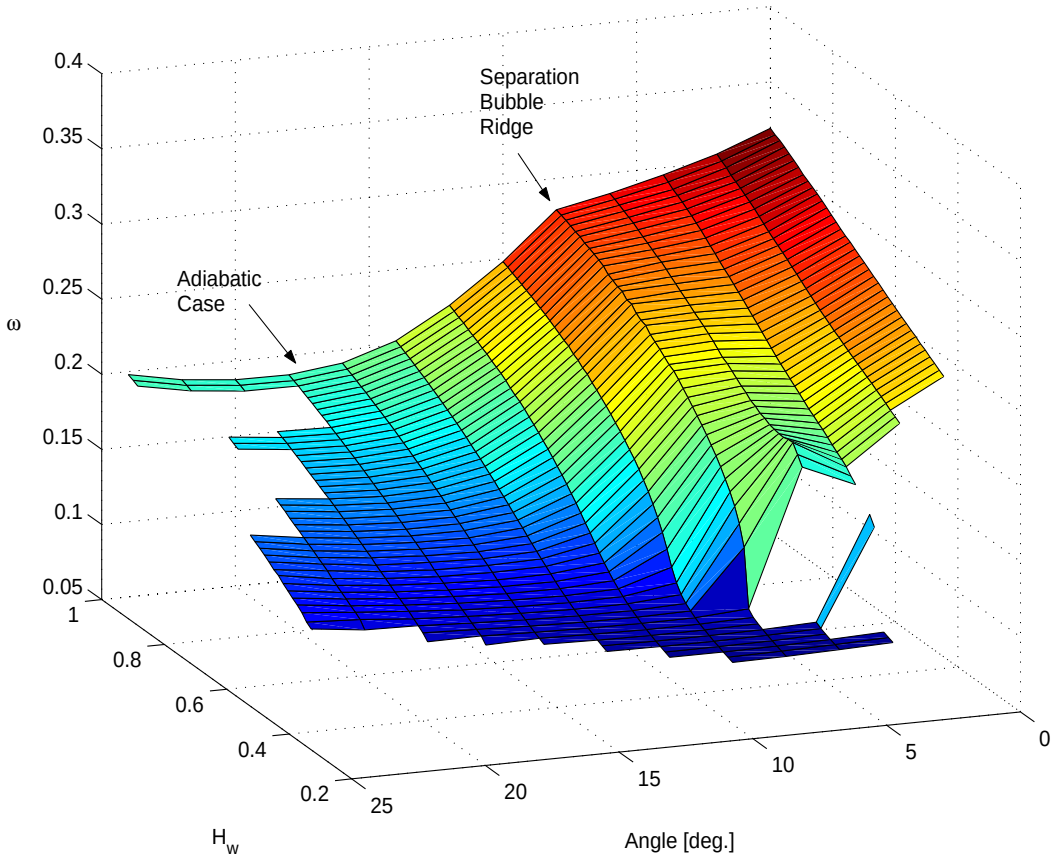

Figure 3-23: Viscous loss performance due to changing H_w and setting angle.

3-24, although a small improvement in heat-exchange is evident at low setting angles. As seen before, the total-enthalpy change varies linearly with H_w.

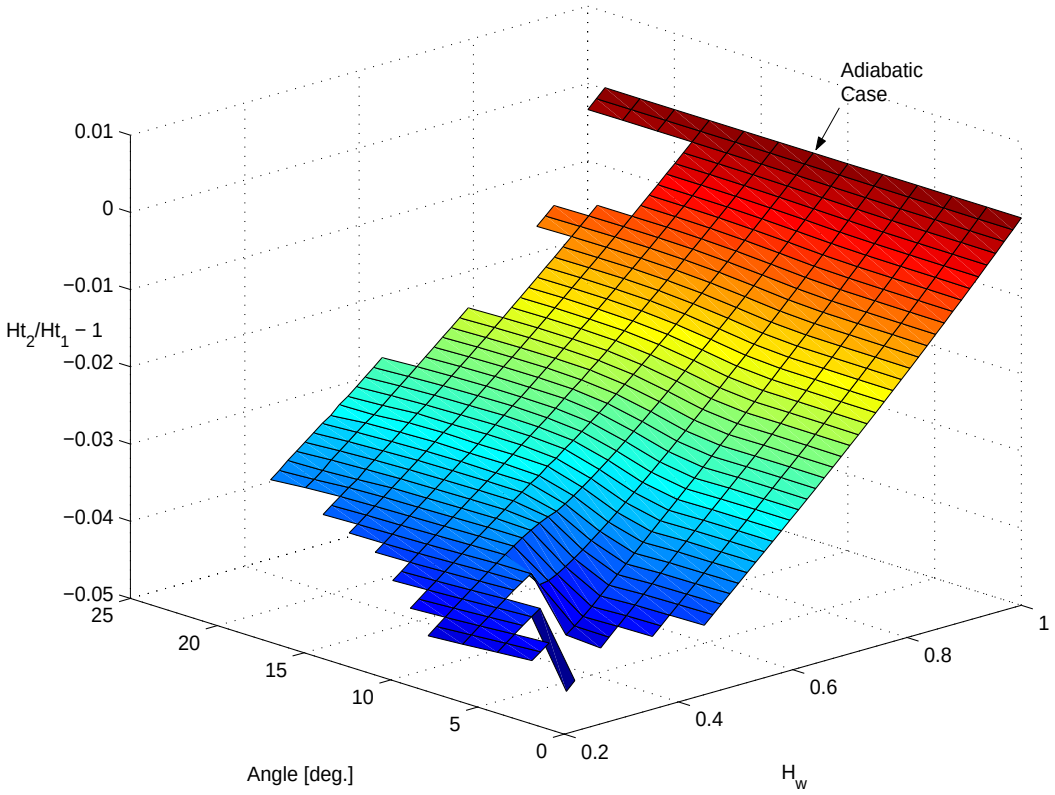

Figure 3-24: Heat-transfer performance due to changing H_w and setting angle.

After reviewing the large 4D parameter space, it is clear that a parameter must be held constant in order to properly apply synergistic design to real flow situations. Since the power plant cooling cycle and steam requirements utilize water, its thermodynamic state is important to know before settling H_w. This information is readily available, thereby reducing the 4D parameter space to three degrees of freedom in the optimum configuration selection. The design space slices conducted at constant H_w will serve as a foundation for applied synergistic design hereafter.

Chapter 4

Applied Synergistic Design

The application of synergistic design in a diffusing heat-exchanger must utilize the numerical results from chapter 3. In the following sections, preliminary design considerations for specific heat-transfer requirements are discussed. A baseline industrial system is then introduced for means of comparison against a synergistic design. Stage-by-stage design case studies are then presented for the power plant that requires saturated vapor steam and superheated steam. In addition to these initial diffusing heat-exchanger designs, alternative design considerations are outlined based on limitations in the current design model, as well as other detailed design points.

4.1 Preliminary Design Spectrum Based on Heat-Transfer Requirements

Since the synergistic design concept seeks to provide adequate cooling performance in a cogeneration plant, the design configuration is driven by heat-transfer requirements. Once the specific steam production requirements are known, the plant designer can utilize figure 3-13 to select a blade cascade configuration that provides adequate cooling performance. At constant $H_{t_2}/H_{t_1} - 1$, set by the cooling requirements, a range of blade solidity is found that provides the same heat-transfer. Therefore, the design space is narrowed to a selection of pitch, chord and setting angle that provides

approximately equal values of δ^*/s. The designer is at liberty to use an additional constraint, such as coolant flow area or structural limitations, to then select the appropriate blade geometry.

Figure 4-1 displays a range of blade geometries (ordered by increasing pitch) that yield $H_{t_2}/H_{t_1} - 1 = -0.01$. Figure 4-2 provides a similar cascade spectrum for $H_{t_2}/H_{t_1} - 1 = -0.04$. These two cooling requirements give examples of a reduced design space. A designer can conduct trade-studies based on other system performance parameters at this point, such as a compromise between material costs and chord, that narrow the preliminary design spectrum to an optimum candidate cascade. This process is appropriate for meeting C_p or ω requirements as well. For example, if C_p is considered, a designer notes that the third case in figure 4-2 exhibits the most pressure loss. This cascade spectrum then informs the designer that lower pressure loss is achieved by a higher setting angle (as in the first case in figure 4-2).

The presentation of a candidate diffusing heat-exchanger is based on this preliminary design methodology in the following sections.

4.2 Industrial Cogeneration: Solar Turbine Titan 130 STAC

The cogeneration industry employs numerous examples of gas-turbine and heat generation systems. Solar Turbines, a Caterpillar company, is a well-known design and manufacturing company that sells cogeneration systems. Among their various products, distinguished by power and steam production capabilities, their Titan 130 gas-turbine with Heat-Recovery Steam Generator (HRSG) and Steam-Turbine Assisted Cogeneration (STAC) systems provide high-power electricity generation and steam for processing. As an example of a mid-range level power generator, the STAC system was used as a baseline configuration for performance comparisons in this study.

Solar Turbines provided ample design information to conduct a preliminary thermodynamic cycle analysis of its Titan 130 gas-turbine, HRSG and STAC systems.

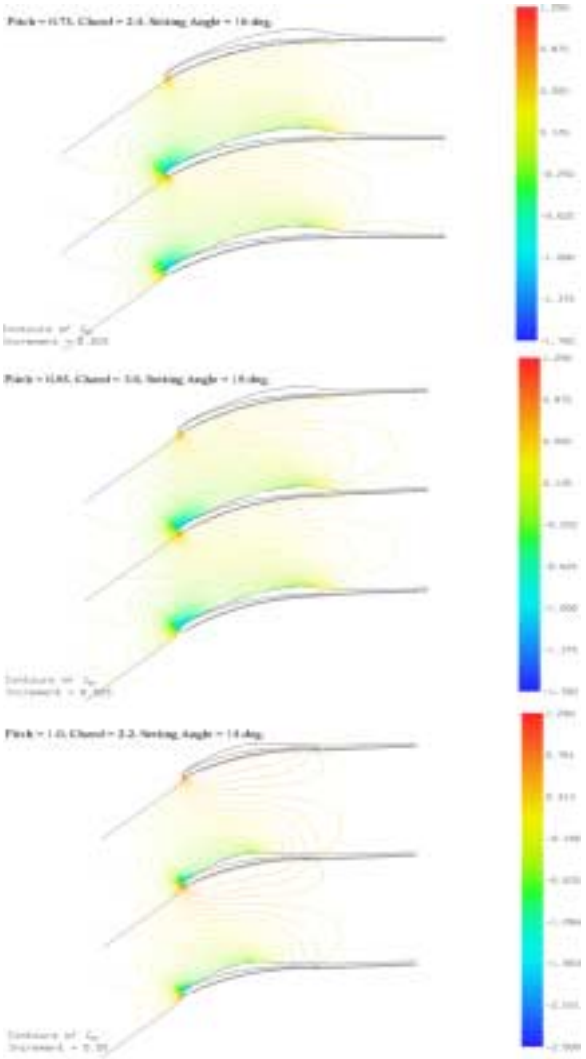

Figure 4-1: An example of blade geometries that represent the design spectrum providing $H_{t_2}/H_{t_1} - 1 = -0.01$.

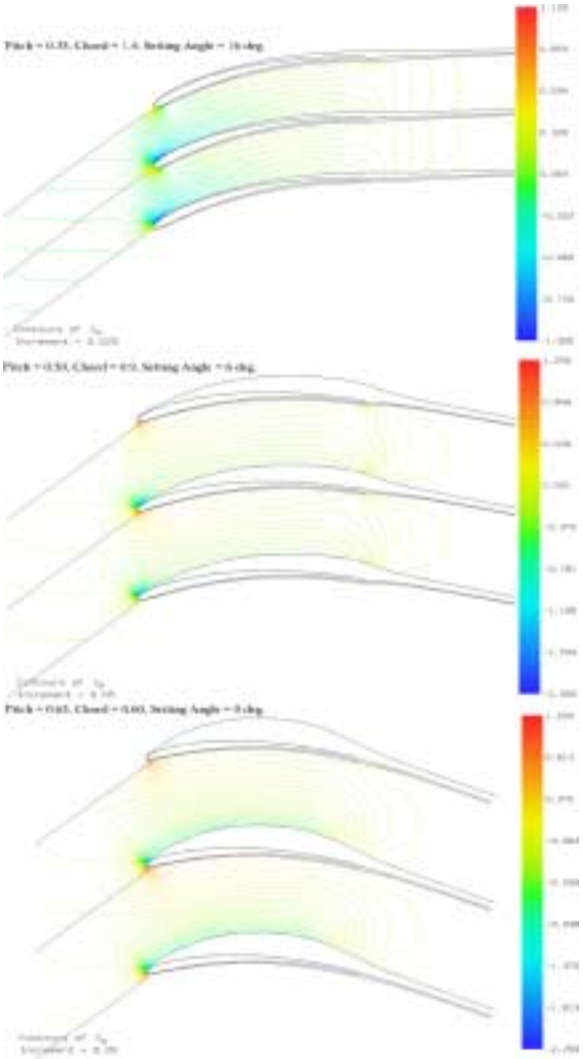

Figure 4-2: An example of blade geometries that represent the design spectrum providing $H_{t_2}/H_{t_1} - 1 = -0.04$.

The cycle calculation results used in this study are summarized in appendix A tables A.2 through A.6. These results provided the basis for diffusion and heat-exchange performance scrutiny against the synergistic design concept.

4.3 Performance Trade-Offs in Synergistic Design

Drela noted that heat-exchange improves as the momentum and thermal boundary-layers begin to merge within radiator passages; however, a maximum was reached when decreasing pitch caused greater viscous loss (due to skin friction) than heat-exchange [2, p. 177]. A similar outcome was obtained in chapter 3, where low pitch values allowed higher heat-transfer rates at the expense of greater viscous losses (see figures 3-17 and 3-18).

It is also evident that a trade-off exists between heat-transfer rates and viscous losses at different blade chord lengths. Figures 3-20 and 3-21 show this trade-off, where low chords yield lower Reynolds numbers to improve the heat-transfer coefficient; yet this causes an increase in viscous losses (lower Reynolds number indicates a higher viscous to inertia force balance in the boundary-layer). The same conclusion is found when reviewing the effect of setting angle on heat-transfer and viscous losses in figures 3-23 and 3-24.

In this synergistic design, it is apparent that low Reynolds number, low pitch and low setting angle provide the highest heat-transfer rates and, conversely, high Reynolds number, high pitch and high setting angle result in the best C_p performance. Therefore, the synergistic character of the diffusing heat-exchanger is one dimensional, in that only C_p benefits from heat-transfer; in order for heat-exchange to improve, C_p performance must be sacrificed. The reduction in diffusion capability is possible at low pitch values, for example, when the momentum boundary-layers reduce the cross-sectional flow area in the core and cause acceleration.

Applying the diffusing heat-exchanger to a gas-turbine exhaust system and STAC requires proper annular blade-row staging requirements. The two requirements for any given stage are

1. Maximize C_p

2. Minimize $H_{t_2}/H_{t_1} - 1$ (negative)

These requirements are linked to the performance trade-offs. In order to see what stage scheduling is appropriate for optimal system performance, the turbine exhaust conditions must be considered. The high turbine exhaust velocity would intuitively require diffusion before heat-transfer is pursued. At the expense of lower heat-transfer rates, high diffusion stages would augment the total C_p between turbine exhaust and the stack inlet, which is calculated to be approximately 0.8 for the Titan 130 STAC setup. If $C_p > 0.8$ is achieved, then the additional aft stages could provide the necessary cooling and suffer a pressure loss that brings the net C_p to 0.8, or above. In this system configuration, the current design C_p is met without a long diffusion tunnel.

The stages dedicated to heat-transfer can also be set to function as economizers, evaporators and superheaters. Diffusing stages providing low cooling rates may have the net effect of a single economizer. A succeeding stage can function as an evaporator, while any additional stages superheat the steam already produced. The number of cooling stages is set by the plant steam processing needs, usually defined as a saturated steam or superheated vapor exit temperature. A limit on superheating is imposed, though, by the wall-enthalpy ratio. As higher steam temperatures (i.e., blade wall temperatures) are created, the core flow total temperature diminishes. These temperatures quickly approach one another, making $H_w \rightarrow 1$, and cause negligible increases in steam temperature thereafter. The Titan 130 STAC design performs at $H_{t_2}/H_{t_1} - 1 = -0.473$, and serves as a maximum value that the synergistic design concept should obtain.

4.4 System Design Configurations

Two diffusing heat-exchange systems were devised using a modified version of the automation scripts running MISES. These scripts permitted optimization of each

subsequent stage by taking into account the increase in coolant enthalpy, reduction in core flow velocity and temperature, increasing core pressure and decreasing Mach number. Pitch, chord and setting angle were varied at each stage until the highest C_p was obtained at the initial stages, followed by the appropriate heat-exchange for water evaporation and steam superheating. Compressed water and saturated steam tables were used to determine the coolant thermodynamic state at each stage exit.

Figure 4-3 shows the C_p (right plot) and cooling (left plot) performance of a 12 stage diffusing heat-exchanger (configuration **A**). The constant q lines represent the ideal case of constant $H_{t_2}/H_{t_1} - 1$ performance at each stage, where (after stage number n) the net cooling rate is:

$$H_{t_n}/H_{t_1} - 1 = \prod_{i=1}^{n-1} \left(\frac{T_{t_{i+1}}}{T_{t_i}} \right) - 1. \tag{4.1}$$

The constant p lines in the C_p plot represent the ideal case of constant p_2/p_1 at each stage, making the net C_p (after stage number n):

$$C_{p_{n,1}} = \frac{\prod_{i=1}^{n-1} \left(\frac{p_{i+1}}{p_i} \right) - 1}{\frac{p_{t_1}}{p_1} - 1}. \tag{4.2}$$

A horizontal solid-line on both the left and right plots of figure 4-3 delineates the Titan 130 STAC baseline performance for comparison. In order to perform adequate diffusion, stage #1 requires specific attention. High turbine exhaust velocities may promote transonic conditions that are very sensitive to blade geometry. Furthermore, the best C_p obtained by any individual stage is that found at stage #1. This is a consequence of the dwindling kinetic-energy that is available for static-pressure rise at later stages. If a maximum possible C_p is not obtained at stage #1, then, at best, the succeeding stages would match the Titan 130 diffusion (between turbine exit and stack inlet).

After six stages, a maximum net C_p was reached. Up to this point, the cooling rates provided the total coolant enthalpy increase of an economizer. The next stage, #7, was optimized as an evaporator. A pressure drop was created at this stage, yet

insufficient to fall below the Titan 130 STAC threshold. More importantly, this stage brought the diffusing heat-exchanger to the same performance level as the Titan configuration. It was noteworthy to point out that subsequent stage additions provided superheated steam (at 125 psia). The baseline Titan configuration was designated to provide saturated vapor steam conditions ($T_w = 344F$), whereas the final superheated steam temperature was $T_w = 628F$ in the diffusing heat-exchanger. Approximately equal C_p performance was obtained between the Titan and the new concept design.

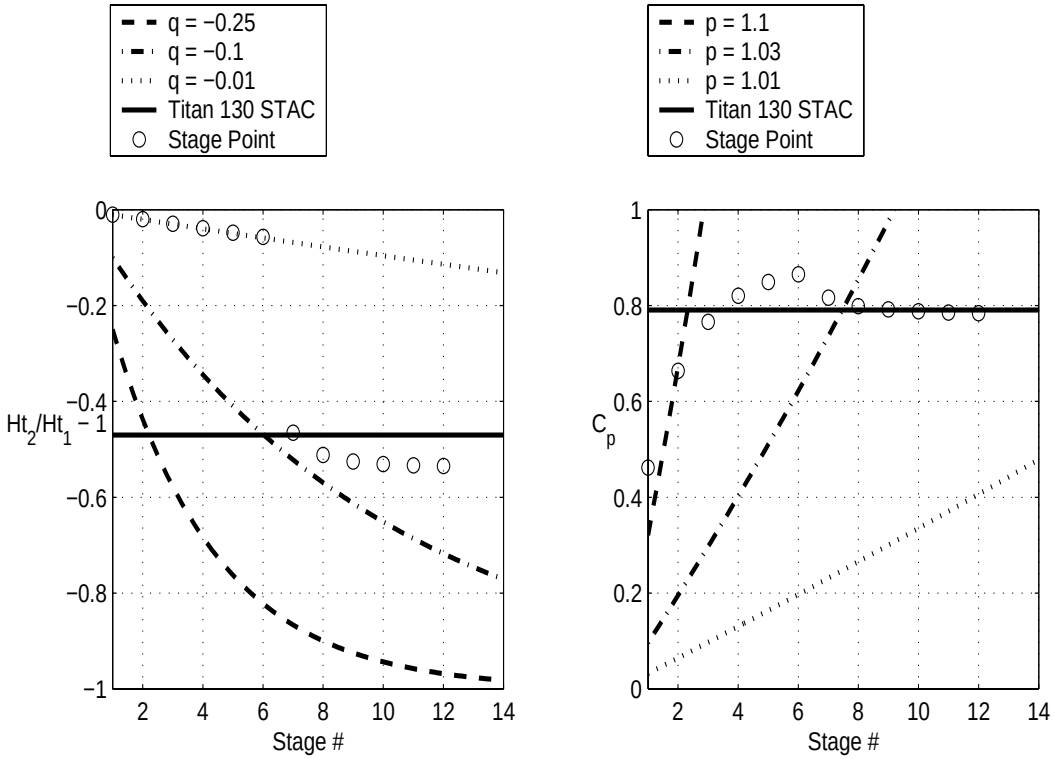

Figure 4-3: Performance comparisons between the Titan 130 STAC and the diffusing heat-exchanger configuration **A**.

The spatial variation of thermodynamic parameters between stages was plotted in figure 4-4. The abrupt change in T_t was attributed to the evaporator stage; also, the H_w values at subsequent stages quickly approached 1 and realized negligible cooling rates. A small acceleration of the core flow was apparent by the small drop in static-pressure during evaporation and superheating.

In figure 4-5, a second configuration (**B**) is shown. This illustrates the shortest

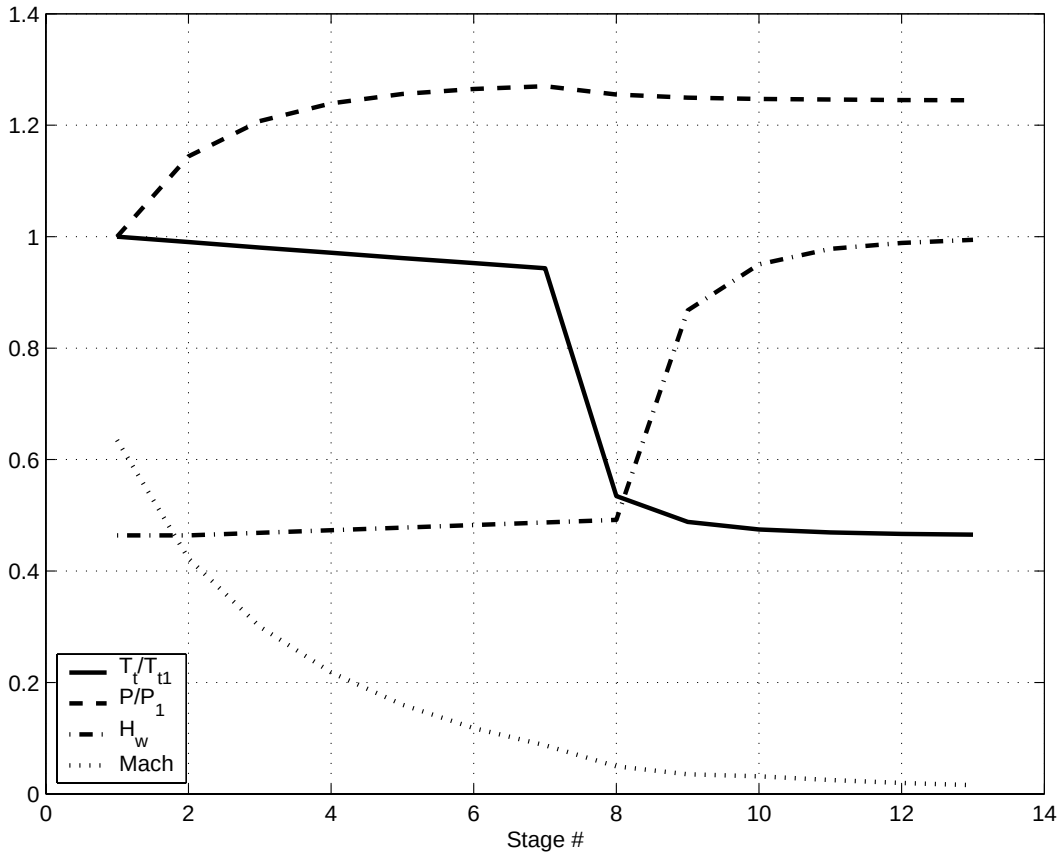

Figure 4-4: Thermodynamic variations between stages in the diffusing heat-exchanger configuration **A**.

possible diffusing heat-exchanger, for the Titan 130 STAC conditions, because stage #7 combines evaporation and superheating while matching the C_p performance. The final superheated steam temperature is $T_w = 1116F$ and the associated steam exit wall-enthalpy ratio approaches $H_w = 1$. In reality, it is possible that the blade H_w distribution may contain $H_w = 1$ forward of the trailing edge, causing a lower steam exit temperature. A higher-fidelity model is required to iterate the stage geometry in order to have $H_w \rightarrow 1$ near the trailing edge. Ideally, a subsequent stage contains $H_w > 1$, which negates attempts at cooling further. Note that stages #1 through #6 provide the same economizer and diffusion performance as configuration **A** in figure 4-3.

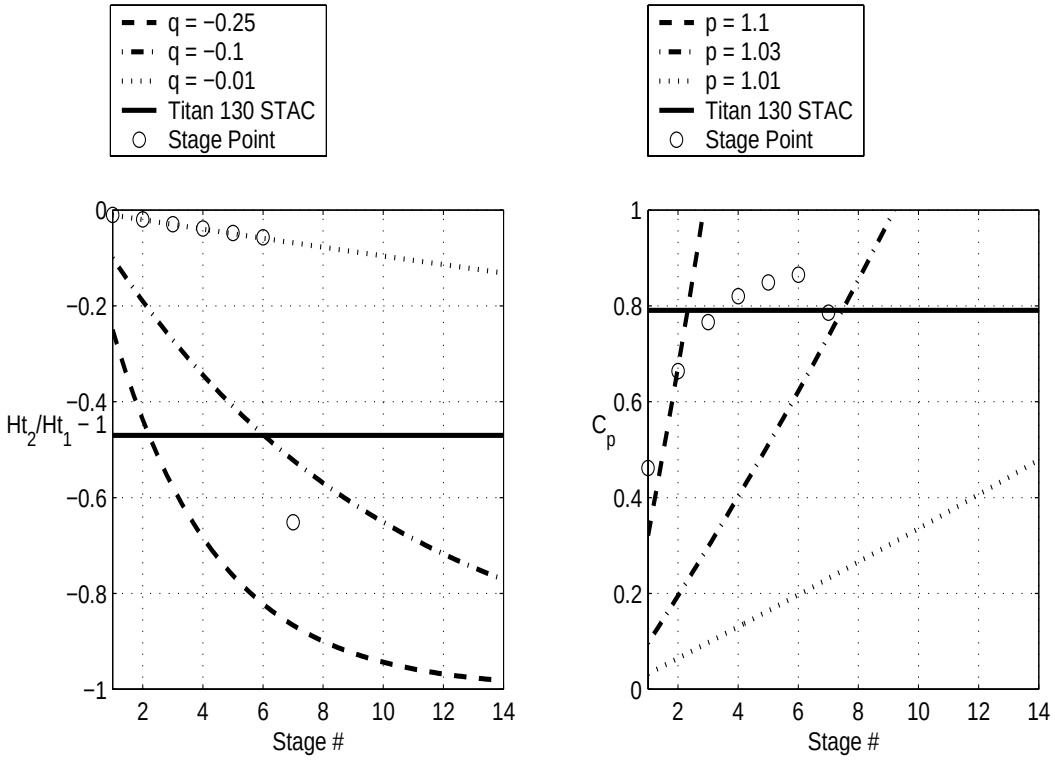

Figure 4-5: Performance comparisons between the Titan 130 STAC and the diffusing heat-exchanger configuration **B**.

Finally, figure 4-6 depicts the thermodynamic evolution between the stages of configuration **B**. There is very little change in H_w up to stage #7, meaning that the coolant and core temperatures change by similar multipliers. This configuration

may be improved if superheater stages were placed in-between the diffuser stages, where the core temperature is higher. Only small increases in coolant temperature may be feasible, though. In addition, higher steam temperatures are usually achieved at higher system pressures. In this configuration, however, a relatively low coolant pressure was maintained despite the superheating capabilities. This can be compared to typical system pressure and steam temperature profiles of industrial cogeneration systems in table 4.1, found in Li & Priddy [3, p. 545].

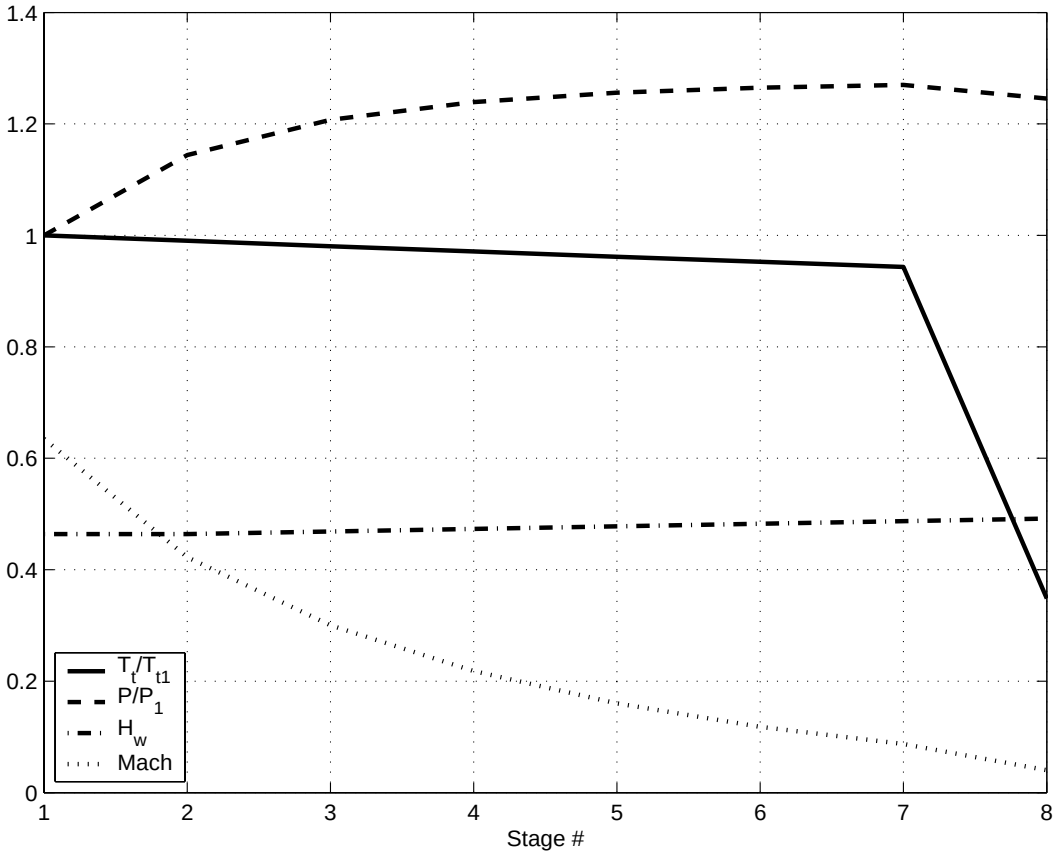

Figure 4-6: Thermodynamic variations between stages in the diffusing heat-exchanger configuration **B**.

A summary of the blade geometries used to create the configuration **A** and **B** performance plots is found in table 4.2. Large pitch and chord values were used for diffusion, as expected, whereas small pitch and chord values were used for cooling. The higher setting angles provided maximum diffusion, via turning, in stages #1

Table 4.1: Common Steam Conditions for Waste Heat Boilers (Heat-Exchangers)

Steam Pressure (psia)	**Temperature (F)**
150	450
250	550
400	650
600	750
850	825
1000	900
1250	950

through #6 and lower angles allowed better heat-exchange in stages #7 and beyond. Figure 4-7 portrayed C_p contours at stage #1. Stage #7 in configuration **B** was optimized to yield $H_w \geq 1$ in subsequent stages (cooling limit). C_p contours at stage #7 were shown in figure 4-8, which contrasted to the diffusion stages as a result of the low pitch, and indicated flow acceleration. Yet stages #10 through #12 in configuration **A** needed to compensate cooling for diffusion in order to match the Titan C_p threshold during superheating.

Table 4.2: Blade geometry summary for configurations **A** and **B**.

	Configuration A			**Configuration B**		
Stage #	Pitch	Chord	Setting Angle	Pitch	Chord	Setting Angle
1	1.00	3.25	18.0	1.00	3.25	18.0
2	1.00	3.25	18.0	1.00	3.25	18.0
3	1.00	3.25	18.0	1.00	3.25	18.0
4	1.00	3.25	18.0	1.00	3.25	18.0
5	1.00	3.25	18.0	1.00	3.25	18.0
6	1.00	3.25	18.0	1.00	3.25	18.0
7	0.12	0.25	17.0	0.10	0.20	-4.0
8	0.12	0.50	17.0			
9	0.12	0.60	-12.0			
10	0.12	0.75	0.0			
11	0.12	0.75	0.0			
12	0.12	0.75	0.0			

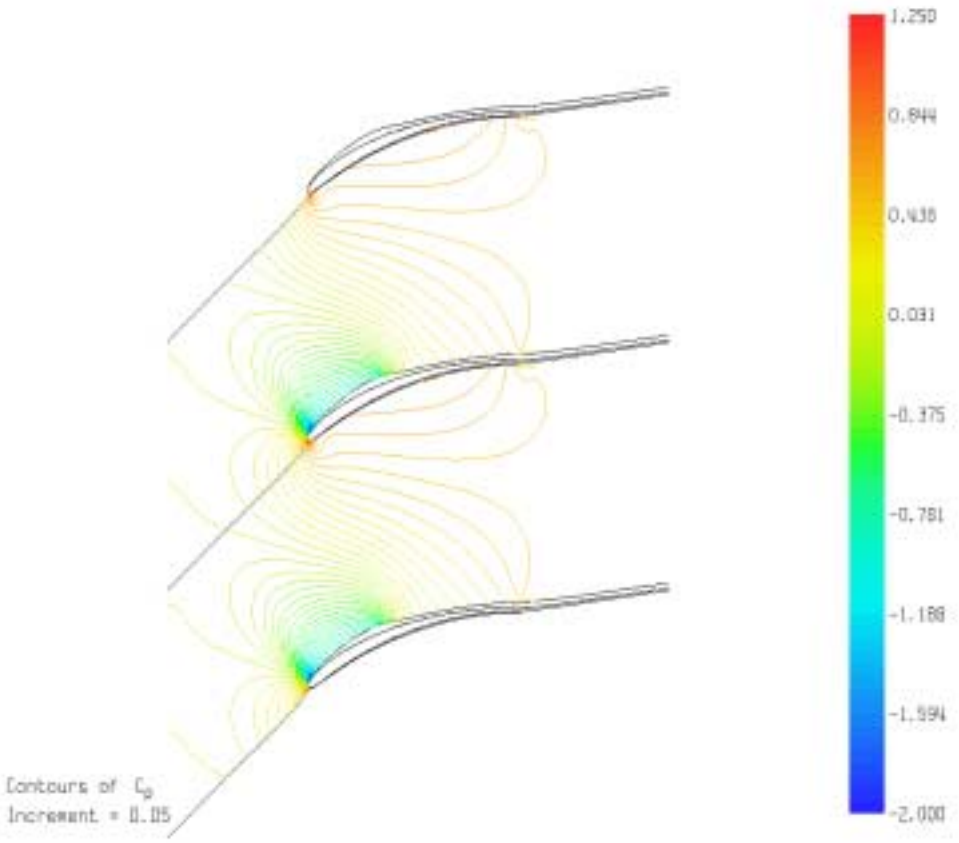

Figure 4-7: C_p contours for stage #1 in configuration **B**.

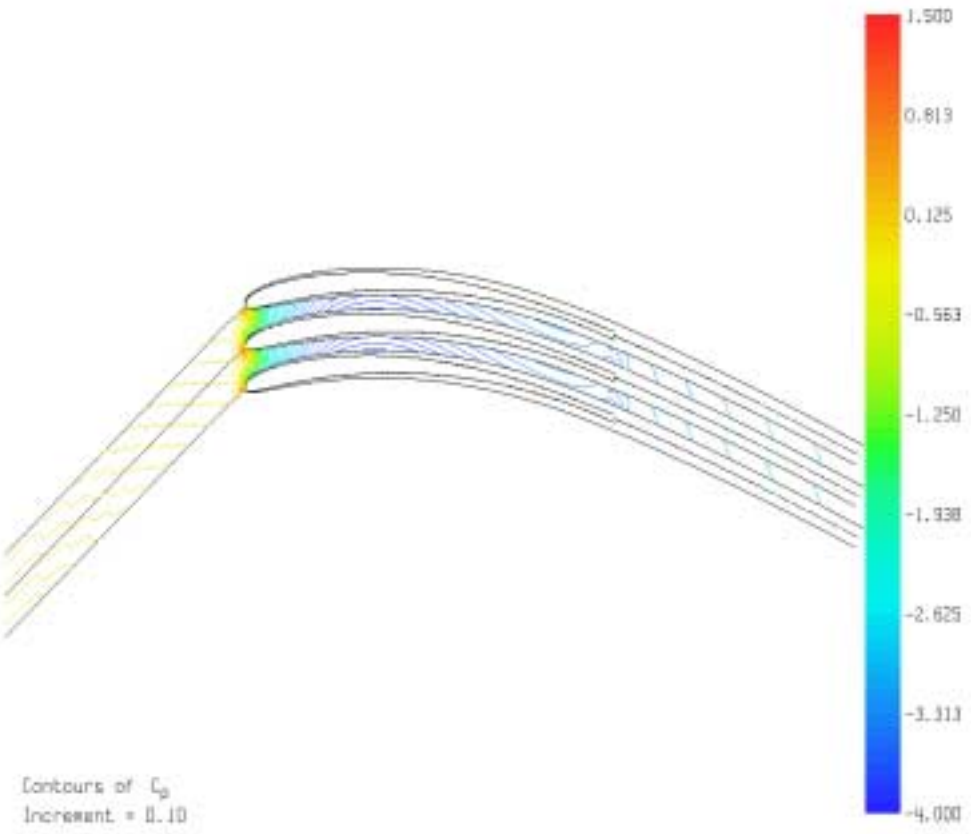

Figure 4-8: C_p contours for stage #7 in configuration **B**.

4.5 Additional System Design Considerations

The diffusing heat-exchanger provided equal or improved performance in comparison to the Titan 130 STAC system. Since 2D numerical tests provided the data for this conclusion, though, 3D flow effects must be taken into account to truly evaluate synergistic design concepts. For example, there may be uneven circumferential cooling in the annulus that generates circumferential pressure-gradients. This added swirl component could jeopardize the annular flow stability as a whole (discussed in 2.3.1). A 3D flow solution could provide the variable cooling by taking into account the changing H_w along the annulus circumference. This flow solver would need to incorporate a solution to the boundary-layer energy equation as well.

Also, scaling the power plant turbine work output may effect diffusion aft of the turbine due to the reduced (higher work output) or increased (lower work output) inlet static-pressure. Additional study would also entail using other steam processing pressures, which could account for lower (or higher) thermal energy availability at the turbine exit. If superheating is not required, then the net C_p of the synergistic design could outperform that of the Titan 130 STAC diffusing tunnel and heat-exchanger because a lower pressure drop would exist. Consequently, the turbine work output could increase to compensate for the added diffusion capability. Inevitably the diffusion/heat-exchanger inlet conditions would change, but an iterative design approach could determine proper system matching.

During each stage geometry iteration, the user was responsible to interpret the MISES output in regards to the sensitivities plotted in sections 3.3.1, 3.3.3, 3.4.1, 3.4.2 and 3.4.3. Gradient-based optimization scripts were tried to automate this brute-force design space search. However, the conflicting objectives and local extrema, introduced by separation bubble phenomena, deterred optimum convergence significantly during automated runs. Furthermore, an external steam-table script was utilized to manually recalculate the changing coolant state after each stage. For these reasons, the initial system designs of synergistic concepts required user understanding of the dominating flow physics at each stage and could not be automated. At constant H_w values,

the design space was reduced to three degrees of freedom, which did not pose an overwhelming burden on the designer.

Depending on the number of annular blades used at each stage, the steam inlet and exit flow paths need design. The two configurations outlined in section 4.4 assume that the coolant enters at stage #1 and is piped through each subsequent stage in series, similar to a multi-pass cross-flow heat-exchanger. These steam paths would ideally be integrated within the structural struts that unite the annular blades.

A schematic of configuration **B** is shown in figure 4-9. The increase in cross-sectional area is constrained by mass flow continuity, making the overall inlet-to-exit area ratio approximately 1:5 and the inlet-to-length ratio about 1:13. Figure 4-10 shows the relative geometrical impact between configuration **B** and the Titan waste heat-recovery system. A substantial savings in overall system size is apparent. Small blade-geometries, though, may pose manufacturing and structural rigidity problems that lead to a design compromise.

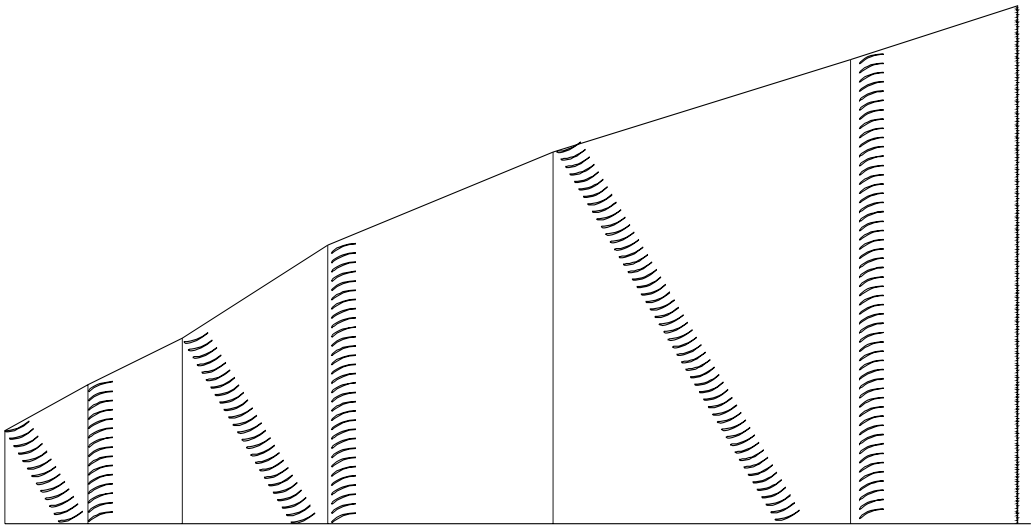

Figure 4-9: Configuration **B** schematic.

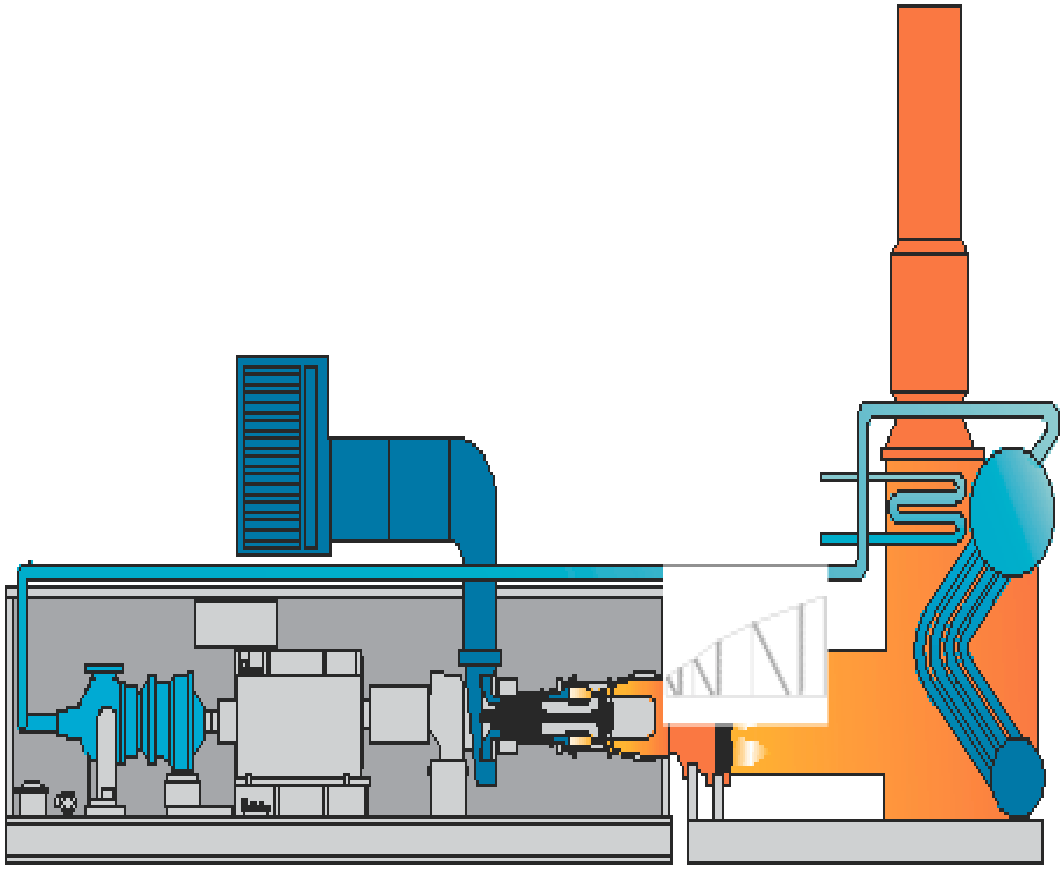

Figure 4-10: Scaled comparison of configuration **B** and the Titan 130 STAC.

Chapter 5

Conclusions

This paper has demonstrated the feasibility and application of synergistic diffusing heat-exchanger design in cogeneration steam production. After motivating the usefulness of synergistic design in cogeneration, the underlying boundary-layer theory was presented to explain how the destabilizing effects of an adverse pressure-gradient were mitigated by cooling in chapter 2. Conceptual validation followed by means of the numerical experiments outlined in chapter 3. These results served as a basis for the system-level design given in chapter 4, where proposed diffusing heat-exchanger configurations were summarized.

The objective of minimizing a geometric footprint was achieved by limiting the number of stages required to properly diffuse and extract thermal energy from a gas-turbine exhaust flow. Compact annular blades with internal convective cooling served the purpose of increasing C_p, which in turn permitted improved heat-transfer in stages downstream. This demonstrated that current diffusion tunnels and large heat-exchange units may be feasibly replaced by compact diffusing heat-exchanger systems that provide equal or better steam production performance. Depending on the steam requirements, diffusion requirements may be surpassed and allow for a higher turbine work output. The two configurations presented in section 4.4 were examples of synergistic design that achieved these results.

Even though the proposed systems were designed using 2D flow analysis without explicit thermal boundary-layer calculations, subsequent finite-difference calculations

on select design cases showed that heat-transfer accuracy is within 5%-10%. Three-dimensional flow features, such as circumferential pressure-gradients and inlet swirl, may inhibit the potential performance presented in this paper. These considerations, as well as the structural annulus design with integrated steam flow paths, need attention in future work. The detailed system design may yield a slight departure in performance from this conceptual and preliminary analysis.

Nevertheless, the synergistic diffusing heat-exchanger design concepts evaluated in this paper show promising performance characteristics that may potentially advance the state-of-the-art in cogeneration plant design.

Appendix A

Solar Turbine Titan 130 Performance Tables

Table A.1: *Solar Turbine* Titan 130 Gas-Turbine STAC Station Inlet Definitions.

Station #	**Component Inlet**
1	Air Filter
2	Compressor
3	Burner
4	Turbine
5	Diffuser
6	STAC
7	Exhaust Stack

Table A.2: *Solar Turbine* Titan 130 Gas-Turbine STAC calculated thermodynamic cycle values.

Station #	T [K]	T_t [K]	P [Pa]	P_t [Pa]	ρ [kg/m^3]	ρ_t [kg/m^3]	$Mach$	u [m/s]
1	288	289	101300	102353	1.200	1.209	0.122	41.36
2	288	289	100562	101606	1.216	1.225	0.122	41.36
3	637	638	1618117	1625698	8.847	8.876	0.082	41.36
4	1334	1450	1598501	1615945	3.853	4.749	0.125	91.22
5	764	826	171774	225390	0.783	0.951	0.635	351.99
6	803	826	204479	225390	0.887	0.951	0.332	188.84
7	431	435	214208	221902	1.733	1.777	0.225	93.65

Table A.3: *Solar Turbine* Titan 130 Gas-Turbine STAC calculated thermodynamic cycle ratios.

Station Ratio	T	T_t	P	P_t	ρ	ρ_t	$Mach$	u
2/1	1.000	1.000	0.993	0.993	1.013	1.013	1.000	1.000
3/2	2.212	2.208	16.091	16.000	7.275	7.246	0.672	1.000
4/3	2.093	2.272	0.988	0.994	0.436	0.535	1.524	2.205
5/4	0.573	0.570	0.107	0.139	0.203	0.200	5.098	3.859
6/5	1.051	1.000	1.190	1.000	1.132	1.000	0.523	0.536
7/6	0.536	0.527	1.048	0.985	1.953	1.869	0.677	0.496

Table A.4: *Solar Turbine* Titan 130 Gas-Turbine STAC results summary.

Performance Results		
$C_{p_{7,5}}$	0.791	
$H_{t_7}/H_{t_5} - 1$	-0.473	
$H_w\ (T_w/T_{t_6})$	0.464	
Compressor Work	1.738e+07	[W]
Turbine Work	3.107e+07	[W]
Steam Turbine	3.114e+06	[W]
Steam Process	1.634e+07	[W]
Thermal Energy Lost	5.627e+06	[W]
Net Efficiency	0.820	
Stack Inlet Temp.	157.61	[C]

Table A.5: *Solar Turbine* Titan 130 Gas-Turbine STAC given information (see [6] and [7]).

Given Information		
$\dot{m}$	49.637	[kg/s]
2/1 P_t Loss	3.00	[in. H_2O]
7/6 P_t Loss	14.00	[in. H_2O]
T_5	491	[C]
Inlet T_w	110	[C]
Net Efficiency	0.820	
Fuel Input	4.042e+07	[W]
Electric Power Gen.	1.369e+07	[W] (w/o Steam Turbine)
Electric Power Gen.	1.680e+07	[W] (w/ Steam Turbine)
Heat Available at #5	2.508e+07	[W]

Table A.6: *Solar Turbine* Titan 130 Gas-Turbine STAC calculation assumptions.

Assumptions	
1	Ideal, adiabatic, isentropic Compressor, Turbine & Diffuser
2	Ideal 1D Constant-Area Burner
3	Constant axial-velocity from inlet to burner inlet
4	Constant specific-heats
5	Sea-level conditions
6	Natural Gas fuel
7	$C_{p_{6,5}} = 0.610$
8	Water coolant & steam pressurized to 125 psia

References

[1] Drela, M., *A User's Guide to MISES 2.53*, Cambridge, MA, 1998.

[2] Drela, M., "Aerodynamics of Heat Exchangers for High-Altitude Aircraft," *Journal of Aircraft*, Vol. 33, No. 2, 1995, pp. 176–184.

[3] Li, K. W. and Priddy, A. P., *Power Plant System Design*, John Wiley & Sons, New York, NY, 1985.

[4] Schlichting, H. and Gersten, K., *Boundary-Layer Theory*, Springer, Berlin, Germany, 8th ed., 2000.

[5] Schlichting, H., *Boundary-Layer Theory*, McGraw-Hill, New York, NY, 7th ed., 1987.

[6] Solar Turbine Incorporated, "Heat Recovery Typical Performance," Datasheet at `www.solarturbines.com`, 2003.

[7] Solar Turbine Incorporated, "Steam Turbine Assisted Cogeneration Systems (STAC)," Datasheet at `www.solarturbines.com`, 2003.

[8] White, F. M., *Fluid Mechanics*, WCB/McGraw-Hill, University of Rhode Island, 4th ed., 1999.

[9] White, F. M., *Viscous Fluid Flow*, McGraw-Hill International Editions, University of Rhode Island, 2nd ed., 1991.

[10] Wilson, D. G., *The Design of High-Efficiency Turbomachinery and Gas Turbines*, The MIT Press, Cambridge, MA, 1984.